

Electroproduction of $p\pi^+\pi^-$ off protons at $0.2 < Q^2 < 0.6$ GeV² and $1.3 < W < 1.57$ GeV with CLAS

G.V. Fedotov,¹ V.I. Mokeev,^{2,1} V.D. Burkert,² L. Elouadrhiri,² E.N. Golovatch,¹ B.S. Ishkhanov,¹
 E.L. Isupov,¹ N.V. Shvedunov,¹ G. Adams,²⁵ M.J. Amarian,²⁴ P. Ambrozewicz,¹¹ M. Anghinolfi,¹⁶
 B. Asavapibhop,³¹ G. Asryan,³⁹ H. Avakian,² H. Baghdasaryan,²⁴ N. Baillie,⁸ J.P. Ball,³ N.A. Baltzell,³³
 V. Batourine,²⁰ M. Battaglieri,¹⁶ I. Bedlinskiy,¹⁸ M. Bektasoglu,²⁴ M. Bellis,^{25,4} N. Benmouna,¹³ A.S. Biselli,¹⁰
 B.E. Bonner,²⁶ S. Bouchigny,^{2,15} S. Boiarinov,² R. Bradford,⁴ D. Branford,⁹ W.K. Brooks,³⁶ S. Bültmann,²⁴
 C. Butuceanu,⁸ J.R. Calarco,³² S.L. Careccia,²⁴ D.S. Carman,² B. Carnahan,⁵ S. Chen,¹² P.L. Cole,^{2,14}
 P. Coltharp,^{12,2} P. Corvisiero,¹⁶ D. Crabb,³⁷ H. Crannell,⁵ V. Crede,¹² J.P. Cummings,²⁵ N.B. Dashyan,³⁹
 E. De Sanctis,¹⁷ R. De Vita,¹⁶ P.V. Degtyarenko,² H. Denizli,³⁴ L. Dennis,¹² K.V. Dharmawardane,²⁴ R.
 Dickson,⁴ C. Djalali,³³ G.E. Dodge,²⁴ J. Donnelly,³⁰ D. Doughty,^{6,2} M. Dugger,³ S. Dytman,³⁴ O.P. Dzyubak,³³
 H. Egiyan,³² K.S. Egiyan,^{39,2,*} P. Eugenio,¹² R. Fatemi,³⁷ R.J. Feuerbach,⁴ T.A. Forest,²⁴ H. Funsten,^{8,*}
 G. Gavalian,²⁴ N.G. Gevorgyan,³⁹ G.P. Gilfoyle,³⁵ K.L. Giovanetti,¹⁹ F.X. Girod,² J.T. Goetz,²⁸ R.W. Gothe,³³
 K.A. Griffioen,⁸ M. Guidal,¹⁵ M. Guillo,³³ N. Guler,²⁴ L. Guo,² V. Gyurjyan,² C. Hadjidakis,¹⁵ J. Hardie,^{6,2}
 N. Hassall,³⁰ F.W. Hersman,³² K. Hicks,²³ I. Hleiqawi,²³ M. Holtrop,³² J. Hu,²⁵ M. Huertas,³³ C.E. Hyde,²⁴
 Y. Ilieva,¹³ D.G. Ireland,³⁰ M.M. Ito,² D. Jenkins,³⁸ H.S. Jo,¹⁵ K. Joo,^{37,29} H.G. Juengst,¹³ J.D. Kellie,³⁰
 M. Khandaker,²² K.Y. Kim,³⁴ K. Kim,²⁰ W. Kim,^{24,20} A. Klein,^{24,20} F.J. Klein,²⁴ A. Klimenko,²⁴
 M. Klusman,²⁵ Z. Krahm,⁴ L.H. Kramer,^{11,2} V. Kubarovsky,²⁵ J. Kuhn,⁴ S.E. Kuhn,²⁴ S. Kuleshov,^{18,36}
 J. Lachniet,⁴ J.M. Laget,^{7,2} J. Langheinrich,³³ D. Lawrence,³¹ T. Lee,³² K. Livingston,³⁰ N. Markov,²⁹
 M. McCracken,⁴ B. McKinnon,³⁰ J.W.C. McNabb,⁴ B.A. Mecking,² M.D. Mestayer,² C.A. Meyer,⁴
 T. Mibe,²³ K. Mikhailov,¹⁸ T. Mineeva,²⁹ R. Minehart,³⁷ M. Mirazita,¹⁷ R. Miskimen,³¹ K. Moriya,⁴
 S.A. Morrow,^{7,15} J. Mueller,³⁴ G.S. Mutchler,^{26,*} P. Nadel-Turonski,¹³ R. Nasseripour,¹¹ S. Niccolai,^{13,15}
 G. Niculescu,^{23,19} I. Niculescu,^{13,19} B.B. Niczyporuk,² R.A. Niyazov,^{2,25} G.V. O'Rielly,³¹ M. Osipenko,^{16,1}
 A.I. Ostrovidov,¹² K. Park,³³ E. Pasyuk,³ C. Paterson,³⁰ J. Pierce,³⁷ N. Pivnyuk,¹⁸ D. Pocanic,³⁷
 O. Pogorelko,¹⁸ S. Pozdniakov,¹⁸ J.W. Price,²⁸ Y. Prok,² D. Protopopescu,³⁰ B.A. Raue,^{11,2} G. Ricco,¹⁶
 M. Ripani,¹⁶ B.G. Ritchie,³ G. Rosner,³⁰ P. Rossi,¹⁷ D. Rowntree,²¹ P.D. Rubin,³⁵ F. Sabatié,⁷ C. Salgado,²²
 J.P. Santoro,^{38,2} V. Sapunenko,² R.A. Schumacher,⁴ V.S. Serov,¹⁸ Y.G. Sharabian,² D. Sharov,¹ J. Shaw,³¹
 E.S. Smith,² L.C. Smith,³⁷ D.I. Sober,⁵ A. Stavinsky,¹⁸ S. Stepanyan,² B.E. Stokes,¹² P. Stoler,²⁵
 K. Stopani,¹ S. Strauch,³³ M. Taiuti,¹⁶ S. Taylor,²⁶ D.J. Tedeschi,³³ R. Thompson,³⁴ A. Tkabladze,^{24,23}
 S. Tkachenko,^{24,23} L. Todor,⁴ C. Tur,³³ M. Ungaro,²⁹ M.F. Vineyard,^{27,35} A.V. Vlassov,¹⁸ L.B. Weinstein,²⁴
 D.P. Weygand,² M. Williams,⁴ E. Wolin,² M.H. Wood,³³ A. Yegneswaran,² L. Zana,³² and J. Zhang²⁴

(The CLAS Collaboration)

¹Moscow State University, Skobeltsyn Nuclear Physics Institute and Physics Department, 119899 Moscow, Russia

²Thomas Jefferson National Accelerator Facility, Newport News, Virginia 23606

³Arizona State University, Tempe, Arizona 85287-1504

⁴Carnegie Mellon University, Pittsburgh, Pennsylvania 15213

⁵Catholic University of America, Washington, D.C. 20064

⁶Christopher Newport University, Newport News, Virginia 23606

⁷CEA-Saclay, Service de Physique Nucléaire, F91191 Gif-sur-Yvette, Cedex, France

⁸College of William and Mary, Williamsburg, Virginia 23187-8795

⁹Edinburgh University, Edinburgh EH9 3JZ, United Kingdom

¹⁰Fairfield University, Fairfield, CT 06824

¹¹Florida International University, Miami, Florida 33199

¹²Florida State University, Tallahassee, Florida 32306

¹³The George Washington University, Washington, DC 20052

¹⁴Idaho State University, Pocatello, Idaho 83209

¹⁵Institut de Physique Nucleaire ORSAY, Orsay, France

¹⁶INFN, Sezione di Genova, 16146 Genova, Italy

¹⁷INFN, Laboratori Nazionali di Frascati, Frascati, Italy 00044

¹⁸Institute of Theoretical and Experimental Physics, Moscow, 117259, Russia

¹⁹James Madison University, Harrisonburg, Virginia 22807

²⁰Kyungpook National University, Daegu 702-701, South Korea

²¹Massachusetts Institute of Technology, Cambridge, Massachusetts 02139-4307

²²Norfolk State University, Norfolk, Virginia 23504

²³Ohio University, Athens, Ohio 45701

²⁴Old Dominion University, Norfolk, Virginia 23529

²⁵*Rensselaer Polytechnic Institute, Troy, New York 12180-3590*

²⁶*Rice University, Houston, Texas 77005-1892*

²⁷*Union College, Schenectady, NY 12308*

²⁸*University of California at Los Angeles, Los Angeles, California 90095-1547*

²⁹*University of Connecticut, Storrs, Connecticut 06269*

³⁰*University of Glasgow, Glasgow G12 8QQ, United Kingdom*

³¹*University of Massachusetts, Amherst, Massachusetts 01003*

³²*University of New Hampshire, Durham, New Hampshire 03824-3568*

³³*University of South Carolina, Columbia, South Carolina 29208*

³⁴*University of Pittsburgh, Pittsburgh, Pennsylvania 15260*

³⁵*University of Richmond, Richmond, Virginia 23173*

³⁶*Universidad Tcnica Federico Santa Mara, Av. Espaa 1680 Casilla 110-V Valparaso, Chile*

³⁷*University of Virginia, Charlottesville, Virginia 22901*

³⁸*Virginia Polytechnic Institute and State University, Blacksburg, Virginia 24061-0435*

³⁹*Yerevan Physics Institute, Yerevan 375036, Armenia*

(Dated: August 14, 2019)

This paper reports on the most comprehensive data set obtained on differential and fully integrated cross sections for the process $ep \rightarrow e'p\pi^+\pi^-$. The data were collected with the CLAS detector at Jefferson Laboratory. Measurements were carried out in the so-far unexplored kinematic region of photon virtuality $0.2 < Q^2 < 0.6 \text{ GeV}^2$ and invariant mass of the final hadron system W from 1.3 to 1.57 GeV. For the first time, nine independent 1-fold differential cross sections were determined in each bin of W and Q^2 covered by the measurements. A phenomenological analysis of the data allowed us to establish the most significant mechanisms contributing to the reaction. The non-resonant mechanisms account for a major part of cross-sections. However, we find sensitivity to s-channel excitations of low-mass nucleon resonances, especially to the $N(1440)P_{11}$ and $N(1520)D_{13}$ states in kinematical dependencies of the 1-fold differential cross-sections.

PACS numbers: PACS : 13.60.Le, 13.40.Gp, 14.20.Gk

I. INTRODUCTION

An extensive research program is currently underway in Hall B at Jefferson Lab with the CLAS detector, focused on studies of nucleon resonances (N^*) in various exclusive channels of meson electroproduction off protons [1, 2, 3]. Part of this effort is aimed at the determination of electrocouplings for an entire spectrum of excited nucleon N^* and Δ^* states versus the photon virtuality $Q^2 = -(e - e')^2$, where e and e' are the 4-momentum vectors of the incoming and scattered electron, respectively. Comprehensive information on resonance electrocouplings and their evolution with Q^2 is needed to probe the spatial and spin structure of the resonance transitions. This information is needed to enhance our understanding of the effective strong interaction that is at the core of internal baryon structure and the decay of baryons. It is also needed to firmly establish the connection of effective degrees of freedom such as a) ‘constituent’ quarks in the binding potential or b) ‘constituent’ quark scattering amplitudes to the elementary quarks and gauge gluons of QCD, the theory of the strong interaction.

In the past five years, single pseudoscalar meson electroproduction has been studied in several exclusive processes, e.g. $p\pi^0$, $n\pi^+$, $p\eta$, $K\Lambda$, and $K\Sigma$, [4, 5, 6, 7,

8, 9, 10, 11, 12, 13, 14, 15, 16, 17, 18], which included differential cross sections with complete polar angle and azimuthal angle distributions, as well as several polarization observables. From these data sets, resonance transition electromagnetic form factors have been determined for the $\Delta(1232)P_{33}$, $N(1535)S_{11}$, and $N(1440)P_{11}$, covering a wide range in Q^2 .

Studies of charged double pion electroproduction off protons represent an important part at this effort. Single and double pion production are the two largest contributors to the total photo- and electroproduction cross sections off protons in the resonance region. The final states produced in these two exclusive channels have considerable hadronic interactions, or so-called final state interactions (FSI). FSI may be determined using the data of experiments with hadronic probes [19]. According to these data, the cross section for the $\pi N \rightarrow \pi\pi N$ reaction has the second largest strength of all of the exclusive channels in the πN interaction. Considerable FSI between the πN and $\pi\pi N$ final states result in substantial contributions to the amplitudes of both single and double pion electroproduction from the electroproduction amplitudes of the other channel. Accounting for these coupled-channel effects is essential in order to get the amplitude description compatible with the constraints imposed by unitarity. Therefore, for N^* studies both in single and double pion electroproduction, information is needed on the mechanisms contributing to each of these channels in order to take properly into account the impact from coupled-channel effects on the exclusive channel cross sec-

*Deceased

tions. The knowledge of single and double pion electroproduction mechanisms becomes even more important for N^* studies in channels with smaller cross sections such as $p\eta$ or $K\Lambda$ and $K\Sigma$ production, as they could be significantly affected in leading order by coupled-channel effects produced by their hadronic interactions with the dominant single and double pion electroproduction channels. Therefore, comprehensive studies of single and double pion electroproduction are of key importance for the entire N^* research program.

The world data on double pion electroproduction in the nucleon resonance excitation region were rather scarce before the data from CLAS became available. Fully integrated cross sections for $\pi\Delta$ isobar channels as a function of the invariant mass of the hadronic system W and photon virtualities Q^2 were available from DESY [20]. However, the data are presented in very large kinematic bins, $\Delta W = 200 - 300$ MeV and $\Delta Q^2 = 0.2 - 0.6$ GeV². Center-of-mass angular distributions for π^- were also measured, but were averaged over a very large intervals in Q^2 from 0.3 to 1.4 GeV². This makes it virtually impossible to determine the nucleon resonance parameters from such measurements.

The first detailed data on charged double pion electroproduction cross sections in the resonance region were obtained with CLAS [21, 23]. The data were collected for $W=1.4 - 2.1$ GeV in 25 MeV bins and for $Q^2 = 0.5 - 1.5$ GeV² in 0.3 GeV² wide bins. The current experiment covers invariant masses of $\pi^-\pi^+$, π^+p and π^-p in each (W, Q^2) bin for $Q^2 = 0.2 - 0.6$ GeV² in 0.05 GeV² wide bins and for $W=1.30$ to 1.57 GeV with 25 MeV bins. In addition, angular distributions for π^- , π^+ , and proton, as well as angular distributions in α_i ($i=1,2,3$) angles (see Sect. V for α_i definitions), were measured. These very detailed measurements are crucial to determine the most significant production mechanisms for this process.

II. ANALYSIS TOOLS

The presence of three hadrons in the final state presents considerable complications in the phenomenological analysis. Efforts to apply partial wave analysis (PWA) techniques to double pion production by electromagnetic probes are limited to photoproduction, where very high statistics data are available [25, 26, 27]. A strong reduction in statistics for individual bins in Q^2 makes application of PWA methods in double pion electroproduction data much more difficult. Moreover, there is no model-independent way to disentangle resonant and non-resonant mechanisms in any given partial wave. Therefore, reaction models are needed to isolate the resonant parts in the double pion production amplitudes and evaluate the N^* electromagnetic transition form factors.

Following the pioneering effort of Ref.[28], several approaches have been developed more recently for the description of double pion photo- and electroproduction in

the resonance region [29, 30, 31, 32, 33, 34, 35]. These efforts were based on a very limited amount of experimental data: mostly on W and Q^2 dependencies for fully integrated cross sections and on invariant mass distributions for various pairs of the final state hadrons. The reaction models used meson-baryon degrees of freedom: N , Δ , π , σ and ρ . Effective meson-baryon Lagrangian operators were constructed based on Lorentz invariance, gauge invariance and crossing symmetry. For the description of experimental data, a limited set of non-resonant meson-baryon diagrams was used with amplitudes calculated from effective Lagrangians together with contributions from several, mostly low-lying nucleon resonances ($M < 1.6$ GeV). A general framework for the implementation of other meson-baryon degrees of freedom was proposed in Ref.[32], but so-far has not been fully realized.

The meson-baryon diagrams in reaction models may account for many partial waves. However, in any reaction model we need to truncate the infinite set of meson-baryon diagrams, keeping just the relevant mechanisms. Moreover, the choice of a particular effective Lagrangian, describing meson-baryon interactions, may be done only at a phenomenological level.

At the distance scale appropriate for the size of hadrons, the amplitudes of effective meson-baryon interactions contributing to the reaction cannot be expanded over a small parameter except for a small kinematic region near threshold W and $Q^2 < 0.2$ GeV² accessible for chiral perturbation theory. This feature makes it impossible to select contributing diagrams based on a perturbative expansion for the entire double pion reaction phase space covered by the CLAS measurements. So-far, no approach has been developed based on a fundamental theory that would allow either a description of an effective Lagrangian or a selection of the contributing meson-baryon mechanisms from basic principles. We therefore have to rely on fits to the now available detailed experimental data sets to develop reaction models that contain the relevant mechanisms.

The large reaction phase space coverage of CLAS data opens up qualitatively new opportunities for the analysis of charged double pion electroproduction. The exclusive channel $ep \rightarrow e'p\pi^+\pi^-$ offers many observables for the analysis. The hadronic final state can be projected on nine independent 1-fold differential cross sections in each W and Q^2 bin. For the first time, all of these observables have become experimentally accessible [21, 22]. By studying the kinematical dependencies of the differential cross section and their correlations we are able to establish the presence and strength of the relevant reaction mechanisms. A phenomenological approach [36, 37, 38, 39, 40, 41, 42, 43, 44] was developed in collaboration between Jefferson Lab and Moscow State University, referred to herein as "JM". This approach is intended to establish all significant mechanisms seen in the observables of charged double pion electroproduction, to isolate the resonant parts of the amplitudes, and to derive the electrocouplings of nucleon resonance transitions

from fits of all measured observables combined.

The CLAS data presented in this paper were collected with binning resolutions over W and Q^2 surpassing by almost an order of magnitude what was achieved in previous measurements before the experiments with CLAS. These data will allow us to extract the electrocoupling amplitudes of the $N(1440)P_{11}$ and $N(1520)D_{13}$ states. A certain advantage of the double pion channel is that the amplitudes of the $N(1440)P_{11}$ resonance do not interfere with the high-mass tail of the $\Delta(1232)P_{33}$ state, as is the case for the amplitudes in single π production.

The behavior of N^* electrocouplings at small photon virtualities is of particular interest. Studies of the magnetic transition form factor for the $\Delta(1232)P_{33}$ in Ref. [45] revealed considerable meson-baryon dressing effects in addition to the 3-quark core contributions. The dressing is expected to decrease with increasing Q^2 . It is most pronounced at $Q^2 < 1.0 \text{ GeV}^2$ [49]. While the role of meson-baryon dressing effects has been studied based on the data on electrocouplings of the $\Delta(1232)P_{33}$ state, for resonances heavier than the $\Delta(1232)P_{33}$, this remains an open question, and is currently being addressed at Jefferson Lab through extensive theoretical efforts [46, 47, 48, 49]. Accounting for these effects is a necessary step to probe quark and possibly gluonic degrees of freedom in baryons. The comparison of constituent quark model predictions [50, 51, 52] with the measured N^* electrocouplings [2, 3], as well as the coupled-channels analysis of the data on reactions with hadronic probes [49], suggest considerable meson-baryon dressing effects at $Q^2 < 0.5 \text{ GeV}^2$ for the $N(1440)P_{11}$ and $N(1520)D_{13}$ electrocouplings. Therefore, the information on these states at low photon virtualities from charged double pion electroproduction may further elucidate the relevant degrees of freedom in resonance excitation at hadronic distance scales.

The data presented in this paper can also provide information on the $p \rightarrow \Delta$ axial transition form factor. Current algebra [53] relates the contact term in the set of non-resonant Born terms for $\pi\Delta$ isobar channels to the axial transition form factors. These contact terms could be fit to the data within the framework of the JM approach [41, 43]. So-far, the $p \rightarrow \Delta$ axial transition form factor has been determined mostly from neutrino-induced reactions [54, 55, 56]. Axial transition form factors offer a complementary view of baryon structure, seen in the axial vector currents, while electroproduction experiments usually access baryon structure through vector currents. Recently, lattice QCD results have become available [57], which make the experimental study of the nucleon axial structure an important topic of hadronic physics.

III. EXPERIMENT

The measurement was carried out using the CEBAF Large Acceptance Spectrometer (CLAS) [58] at the Thomas Jefferson National Accelerator Facility (Jefferson Lab).

CLAS provides almost complete angular coverage in the center-of-mass frame. It is well suited for conducting experiments that require detection of two or more particles in the final state. Such a detector and the continuous beam produced by CEBAF provide excellent conditions for measuring the $ep \rightarrow e'p'\pi^+\pi^-$ cross section by detecting the outgoing electron, proton and at least one pion in coincidence.

A. Apparatus

The main magnetic field of CLAS is provided by six superconducting coils, symmetrically arranged around the beam line, which generate an approximately toroidal field in the azimuthal direction around the beam axis. The gaps between the coil cryostat are instrumented with six identical detector packages, referred to here as "sectors", as shown in Fig. 1. Each sector consists of three regions (Region 1, Region 2, Region 3) of Drift Chambers (DC) [59] to determine the trajectories of the charged particles as they travel from the target outward in magnetic field, a Cherenkov Counter [60] for electron identification, Scintillator Counters (SC) [61] for charged particle identification using the Time-of-Flight (TOF) method, and an Electromagnetic Calorimeter [62] for electron identification. The liquid-hydrogen target was located in the center of the detector. To reduce the electromagnetic background resulting from Møller scattering off atomic electrons, a second smaller normal-conducting toroidal magnet (mini-torus) was placed symmetrically around the target. This additional magnetic field prevented Møller electrons from reaching the sensitive detector volume. A totally absorbing Faraday cup, located at the very end of beam line, was used to determine the integrated beam charge passing through the target. The CLAS detector provides $\approx 80\%$ of 4π solid-angle coverage. The efficiency of detection and reconstruction for single stable charged particles in the fiducial regions of CLAS is greater than 95%. The combined information from tracking in the DC and the SC systems allows us to reliably separate protons from positive pions. Additional constraints for event selection come from the overdetermined kinematics, which allows use of the missing mass technique.

Due to possible slight misalignments in the DC positions and small inaccuracies in the description of the torus magnetic field, the reconstructed momentum and angle of particles may have small systematic deviations from the physical value. To correct these deviations, elastic electron-proton scattering was checked and the electron 3-momenta were corrected to ensure the proper mass peak position for the recoil proton [63]. The proton energy losses in CLAS were estimated from a simulation of proton propagation through the detector materials in kinematics corresponding to charged double pion electroproduction.

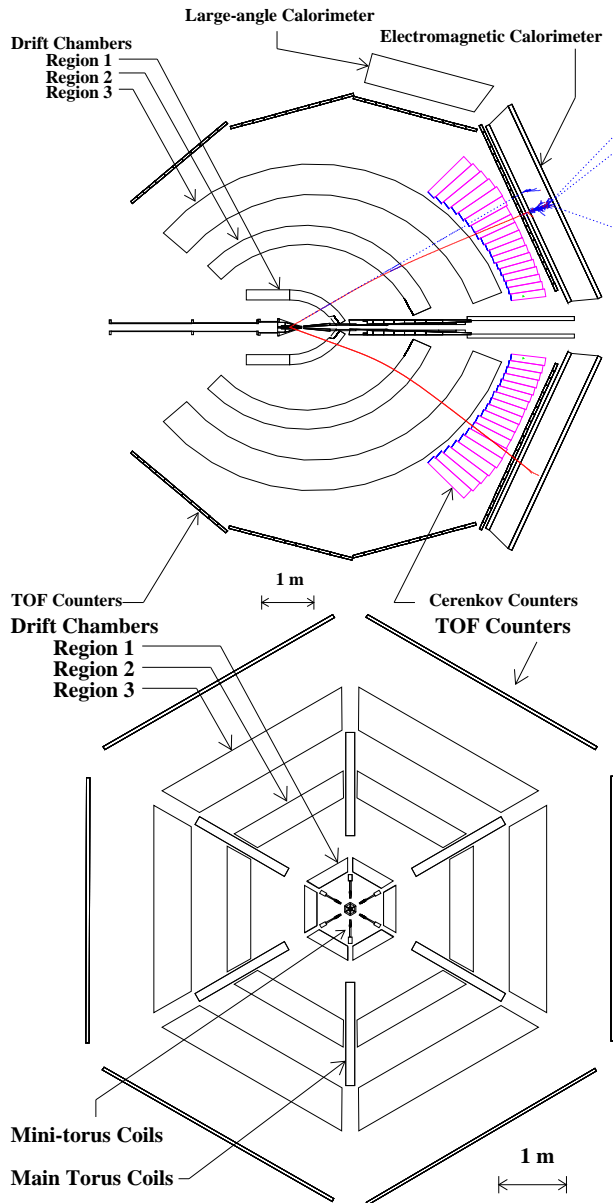


FIG. 1: (color online) Cross-sectional views of the CLAS detector. The top panel shows a cut along the beam line and through the mid-plane of two opposite sectors. The bottom panel shows a cut perpendicular to the beam line and through the nominal target center. Descriptions of the detector elements are given in the text of Sect. III A.

B. Data taking and data reduction

This analysis is based on data taken during the 1999 elc run period. The 1.515 GeV electron beam at a current of 3 nA was incident on a 5-cm-long liquid-hydrogen target corresponding to an instantaneous luminosity of $\sim 4 \times 10^{33} \text{ cm}^{-2}\text{s}^{-1}$. The size of the beam spot at the target was $\sim 0.2 \text{ mm}$, with position fluctuations $< \pm 0.04 \text{ mm}$. The main torus current was set at 1500 A, which created a magnetic field of about 0.8 T at polar angles of 20° that decreased with increasing polar an-

gle. The CLAS event readout was triggered by a coincidence of signals from an electromagnetic calorimeter module and a threshold gas Cherenkov counter in one of the six sectors, generating a total event rate of $\sim 2 \text{ kHz}$. The number of accumulated triggers at these detector settings was about 4.2×10^8 . These data were further analyzed to extract the differential cross sections for the $ep \rightarrow e'p'\pi^+\pi^-$ reaction.

IV. EVENT SELECTION

The $ep \rightarrow e'p'\pi^+\pi^-$ reaction is selected by measuring the scattered electron, as well as the proton and π^+ in the hadronic final state. In the magnetic field configuration used in this measurement, the negatively charged pions have a smaller probability for detection than the positively charged particles. However, the process is kinematically overconstrained and the detection of all particles in the final state is not required for an unambiguous identification of the exclusive reaction. To retain maximum acceptance, we chose to not require detection of the π^- , but infer the presence and kinematics of the undetected π^- by computing the mass of the undetected particle from 4-momentum conservation and its charge from charge conservation. The two other topologies, with either undetected proton or undetected π^+ , have considerably lower rates and were used for systematics studies and for cross checks, but are not included in the determination of the final cross sections.

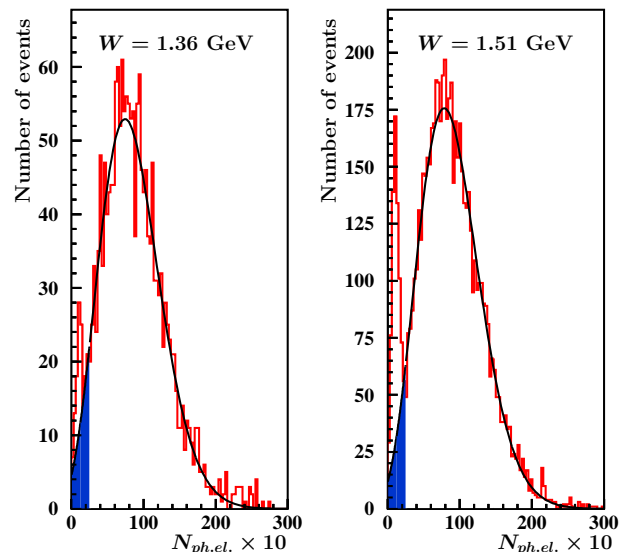


FIG. 2: (color online) Distribution of photoelectrons in the Cherenkov counter for $0.3 < Q^2 < 0.4 \text{ GeV}^2$ in two W bins centered at the values shown in the plot. The curves represent a Poisson fit.

For each event we identify as the electron candidate the first coming negatively charged particle detected in the electromagnetic calorimeter and the Cherenkov counter.

To select true electrons, we apply a cut in the number of photoelectrons ($N_{phe} \geq 2.5$) produced by the Cherenkov light signal in the photomultipliers. This cut also eliminates a small fraction of electrons ($< 6\%$), as shown in Fig. 2. The shadowed areas correspond to the cut-out electrons. A special procedure was developed to account for these electrons in the evaluation of the reconstruction efficiency, based on the extrapolation of the photoelectron spectra into the cut-out areas using a fit based on a Poisson distribution. The quality of electron identification may be seen in Fig. 3, where we display the energies deposited in the outer part of the calorimeter versus the energies deposited in the inner part of the EC, normalized to the momenta of the incoming particles. A spot from minimum-ionizing pions, clearly seen in inclusive electron events (top part of Fig. 3) disappears after applying the described cuts for electron selection (bottom part of Fig. 3).

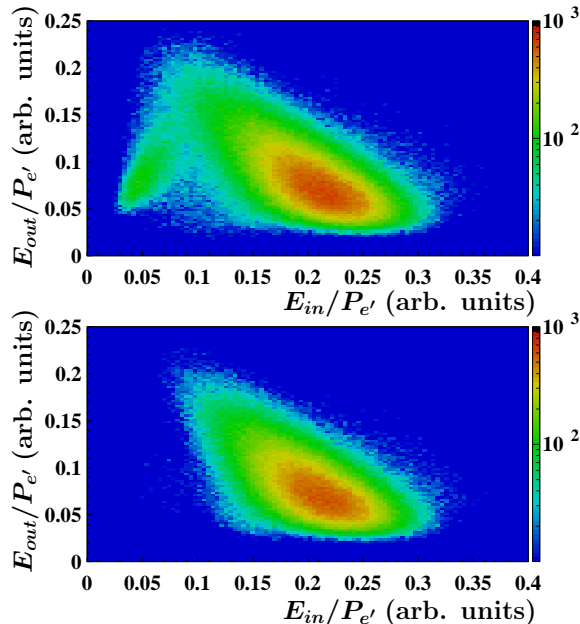


FIG. 3: (color online) Distributions for the energies deposited in the outer part (E_{out}) versus the energies deposited in the inner part (E_{in}) of the EC normalized to the momenta of the outgoing particles ($P_{e'}$). The distribution for the accumulated triggers is shown in the top plot, while the distribution for the events selected, applying the photoelectron cut, is shown in the bottom plot.

Using information from the time-of-flight scintillators and the path length determined by tracking, the particle's velocity (β) was determined. The information from the drift chambers, combined with the known magnetic field, provides a measurement of the particle momentum (p). Relativistic relations between particle mass, momentum and velocity were used in order to determine the particle's mass, allowing us to separate pions, kaons, and protons in the kinematic range covered by the measurement. Fig. 4 shows the velocity versus the momentum

for positively charged particles.

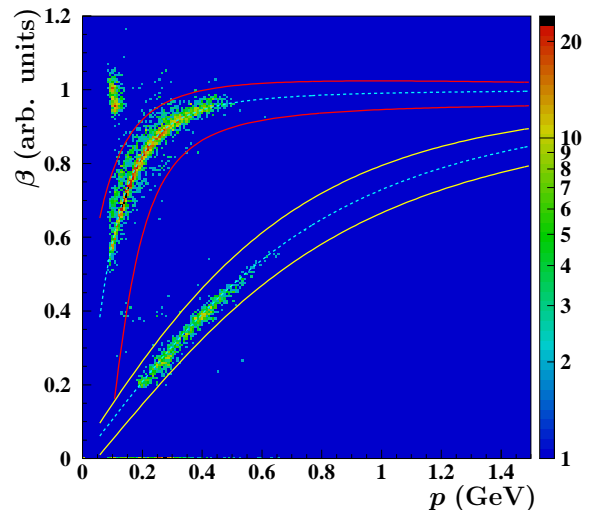


FIG. 4: (color online) β versus momentum for positively charged hadrons; solid curves show the cuts used to identify pions and protons; dashed curves show the explicit β vs p relationships, using the pion and proton mass, respectively. The events near $\beta=1$ and $p=0.1$ GeV are positrons, e.g. from π^0 Dalitz decay. The data were collected in a single scintillator bar.

After identification of the three particles, events were selected with one electron, one proton and one π^+ . The squared missing mass distribution is shown in Fig. 5, which clearly shows the pion mass peak and also indicates that multi-pion background ($> 2\pi$) contributes less than 1 % to the total number of charged double pion events selected by the cuts. The small background is related to the kinematic coverage of our experiment $W < 1.57$ GeV, where the exclusive channels with more than two pions in the final state are suppressed due to their thresholds. The almost negligible contribution from the multi-pion background and the rather small radiative effects (see Sect. V F) allowed us to apply a wide exclusivity cut over the squared missing mass distribution, shown in Fig. 5 by the two arrows, in order to collect the majority of the 2π events.

The CLAS detector has an active detection solid angle smaller than 4π due to the space filled with the torus magnet coils. The angles covered by the torus magnet coils are not equipped with any detection system and therefore give rise to inactive areas. The boundaries of the active areas are not well defined and do not provide regions for particle reconstruction with full reconstruction efficiency. Therefore, for the analysis we accept only events inside specific fiducial areas whose contours are defined by parameterizations of the kinematic variables of each particle. Within these well-defined regions, acceptances and track reconstruction efficiencies are well understood using Monte Carlo simulations.

After all selections have been applied, there remain about 130,000 exclusive $p\pi^+\pi^-$ events. Fig. 6 shows the

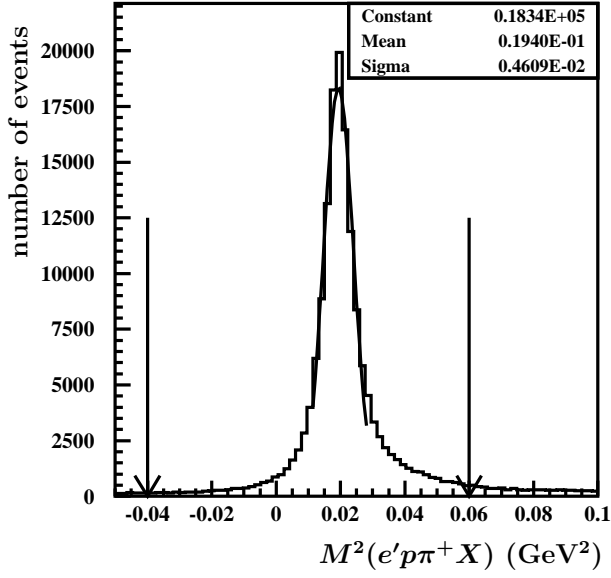


FIG. 5: The distribution of squared missing mass $M^2(e'p\pi^+X)$ (GeV^2). The arrows show the exclusivity cut.

Q^2 versus W distribution for the selected 2π events.

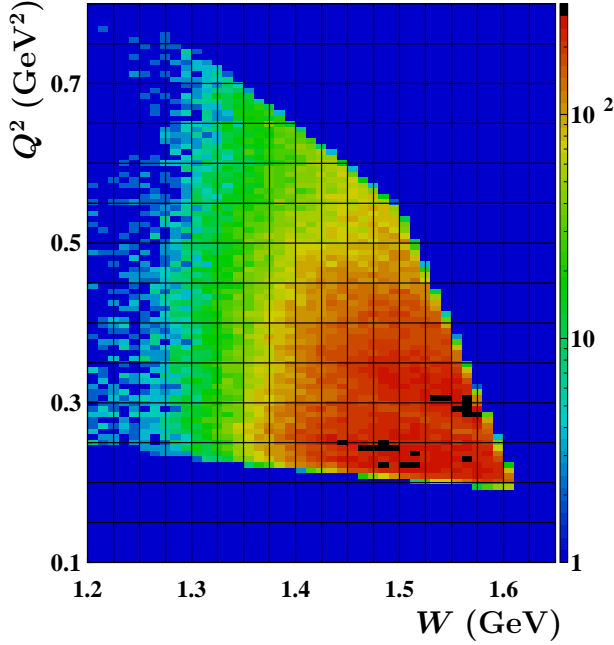


FIG. 6: (color online) Q^2 (GeV^2) versus W (GeV) distribution for the selected 2π events. The grid shows the binning used for the evaluation of the cross section. Only cells inside the allowed phase space were used for that purpose.

V. CHARGED DOUBLE PION ELECTROPRODUCTION CROSS SECTIONS

The kinematics of the 3-body $p\pi^+\pi^-$ final state are unambiguously determined by five independent variables [64]. However, the choice of these variables is not unique. In this section we specify the kinematic variables we employ to describe the $p\pi^+\pi^-$ final state and related phase space element for the 5-fold differential cross section. Note, that the double pion cross sections for virtual photon absorption are 5-fold differential, while the double pion electroproduction cross sections are 7-fold differential, since they contain the additional variables W and Q^2 . Then we describe the procedure to evaluate the 5-fold differential charged double pion cross section from experimental data from the 7-dimensional event distributions. The 5-fold differential cross section contains complete information on double pion production at fixed Q^2 and W . However, the limited statistics do not allow direct study of the 5-fold differential cross sections. Therefore, for the physics analysis we use various 1-fold differential cross sections, obtained by integrating the 5-fold differential cross section over the four other variables.

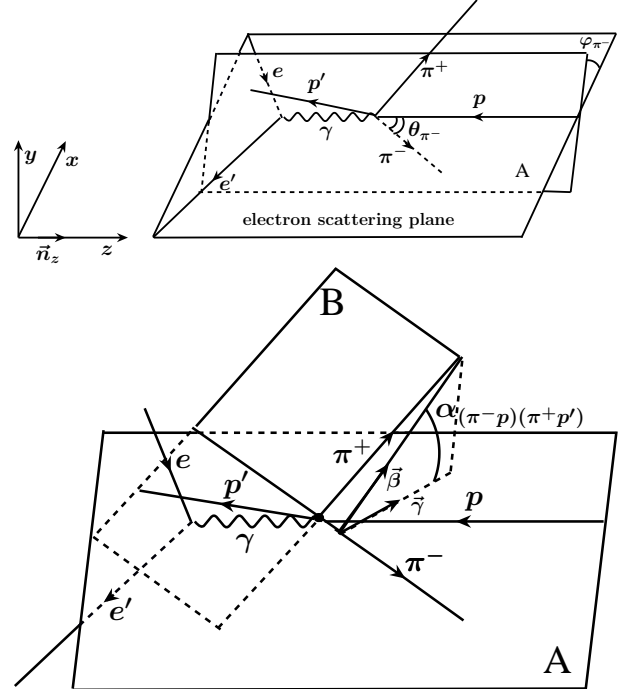


FIG. 7: Kinematic variables for the $ep \rightarrow e'p'\pi^+\pi^-$ reaction (choice 2 in Sect. V A). The top plot shows the π^- spherical angles θ_{π^-} and φ_{π^-} , while the bottom plot shows the angle $\alpha_{(\pi^-p)(\pi^+p')}$ of the plane defined by the momenta of the final $p\pi^+$ pair with respect to the plane comprised by the momenta of the initial proton p and π^- .

A. Kinematic variables

We adopt the following set of variables to describe the 3-body final state:

- invariant mass of the first pair of particles M_{12} ;
- invariant mass of the second pair of particles M_{23} ;
- the first particle solid angle Ω ;
- the angle between two planes: one of them (plane A) is defined by the 3-momenta of the virtual photon and the first hadron, and the second plane (plane B) is defined by the 3-momenta of the two other hadrons (see Fig. 7).

We use three different assignments for the first, second and third final state hadrons:

- invariant mass of the $p\pi^+$ pair, invariant mass of the $\pi^+\pi^-$ pair, the final proton spherical angles θ_p and φ_p and the angle $\alpha_{(pp')(\pi^+\pi^-)}$ between the two planes: B, composed by the momenta of the $\pi^+\pi^-$ pair, and A, composed by the momenta of the initial and final protons (choice 1) ;
- invariant mass of the $\pi^+\pi^-$ pair, invariant mass of the $p\pi^+$ pair, π^- spherical angles θ_{π^-} and φ_{π^-} and the angle $\alpha_{(p\pi^+)(\pi^+\pi^-)}$ between the two planes: B, composed by the momenta of the final state proton p' and π^+ , and A, composed by the initial state proton p and π^- (choice 2);
- invariant mass of the $p\pi^+$ pair, invariant mass of the $p\pi^-$ pair, π^+ spherical angles θ_{π^+} and φ_{π^+} and the angle $\alpha_{(p\pi^+)(p'\pi^-)}$ between the two planes: B, composed of the momenta of the final state proton p' and π^- and A, composed by the initial state proton p and π^+ (choice 3).

The 5-fold differential cross sections were obtained for all three sets of variables. The emission angles for the final particles in the second set of variables are shown in Fig. 7. For the other sets the emission angles are defined in a similar way. In the physics analysis, described in Sect. VI, the second set of variables is used. These variables are suitable for the description of charged double pion electroproduction through a $\pi^-\Delta^{++}$ intermediate state, which represents the main contributor of all isobar channels in the kinematic area covered by our data. The relations between the four momenta of the final state hadrons and the kinematic variables may be found in Appendix A.

B. Evaluation of charged double pion cross sections

The selected double π events were collected in 7-dimensional cells, composed of W , Q^2 , invariant masses

of the first pair M_{12} and the second pair M_{23} of the final state particles, solid angle for the first final state particle, and the angle α_i between the two planes A and B. The cross sections were determined only for those W cells, that are fully inside the kinematically allowed area. Special procedures were developed in order to evaluate the 1-fold differential cross sections for the final state particle invariant mass values near edges of the reaction phase space (see Sect. V D, V E). All frame-dependent variables and the cross sections were evaluated in the center-of-mass frame.

For the second choice of kinematic variables, the 7-fold differential cross sections $\frac{d\sigma}{dW dQ^2 d^5\tau_2}$, $d^5\tau_2 = dM_{p\pi^+} dM_{\pi^+\pi^-} d\Omega_{\pi^-} d\alpha_{[p\pi^-][p'\pi^+]}$ are given by the number of $p\pi^+\pi^-$ events ΔN and efficiencies ϵ in the 7-dimensional cells as:

$$\frac{d\sigma}{dW dQ^2 d^5\tau_2} = \frac{1}{\epsilon \cdot \epsilon_{ch} \cdot R} \frac{\Delta N}{\Delta W \Delta Q^2 \Delta^5\tau_2 L} . \quad (1)$$

The number of events inside the 7-dimensional cells were corrected for contamination from the target walls, which was measured in separate runs with an empty target cell. The efficiency ϵ in any 7-dimensional cell was determined in detailed Monte Carlo simulations. The inactive zones of CLAS and all cuts on phase space used in the event selection were included in the efficiency evaluation. The factor ϵ_{ch} accounts for the Cherenkov counter efficiency, which was determined separately. R accounts for radiative corrections. The integrated luminosity L was determined from the total beam charge Q measured in the Faraday cup, combined with the information on target length and target density:

$$L = Q \frac{l_t D_t N_A}{q_e M_H} , \quad (2)$$

where q_e is the elementary charge, D_t is the density of hydrogen ($D_t = 0.073$ g/cm³), l_t is the length of the target ($l_t = 5$ cm), M_H is the molar density of hydrogen ($M_H = 1$ g/mol), and N_A is Avogadro's number. The luminosity value was verified by reproducing elastic ep cross sections with the same data set. A comparison of the elastic ep scattering cross sections determined from our data with a parameterization of world data given in Ref. [65] showed agreement within better than 5 %. ΔW and ΔQ^2 are bins over W and Q^2 , and $\Delta^5\tau_2$ represents the element of hadronic 5-dimensional phase space for the second choice of kinematic variables:

$$\Delta^5\tau_2 = \Delta M_{p\pi^+} \Delta M_{\pi^+\pi^-} \Delta \cos(\theta_{\pi^-}) \Delta \varphi_{\pi^-} \Delta \alpha_{(p\pi^-)(p'\pi^+)} . \quad (3)$$

The 7-fold differential cross sections for the other two choices of kinematic variables listed in Sect. V A may be obtained from eq. (3), by substituting the phase space

element $\Delta^5\tau_2$ with:

$$\Delta^5\tau_1 = \Delta M_{p\pi^+} \Delta M_{\pi^+\pi^-} \Delta \cos(\theta_p) \Delta \varphi_p \Delta \alpha_{(pp')(\pi^-\pi^+)}; \quad (4)$$

$$\Delta^5\tau_3 = \Delta M_{p\pi^-} \Delta M_{p\pi^+} \Delta \cos(\theta_{\pi^+}) \Delta \varphi_{\pi^+} \Delta \alpha_{(p\pi^+)(p'\pi^-)}.$$

In the single photon exchange approximation, the 7-fold differential electron scattering cross section is related to the hadronic 5-fold differential cross section as [66]:

$$\frac{d\sigma}{dM_{p\pi^+} dM_{\pi^+\pi^-} d\Omega_{\pi^-} d\alpha_{(p\pi^-)(p'\pi^+)}} = \frac{1}{\Gamma_v} \frac{d\sigma}{dW dQ^2 dM_{p\pi^+} dM_{\pi^+\pi^-} d\Omega_{\pi^-} d\alpha_{(p\pi^-)(p'\pi^+)}} , \quad (5)$$

where Γ_v is virtual photon flux, given by

$$\Gamma_v = \frac{\alpha}{4\pi} \frac{1}{E_b^2 M_p^2} \frac{W(W^2 - M_p^2)}{(1 - \varepsilon)Q^2} , \quad (6)$$

and α is the fine structure constant, E_b is the beam energy, M_p is the proton mass, and ε is the virtual photon transverse polarization given by

$$\varepsilon = \left(1 + 2 \left(1 + \frac{\nu^2}{Q^2} \right) \tan^2 \left(\frac{\theta_e}{2} \right) \right)^{-1} , \quad (7)$$

where ν is the virtual photon energy and θ_e is the electron scattering angle in the laboratory frame. W , Q^2 and θ_e were taken at their respective bin centers.

The limited statistics do not allow use of correlated multi-fold differential cross sections for physics analysis. In the physics analysis we instead used 1-fold differential cross sections, obtained after integration of the 5-fold differential cross sections over four kinematic variables. The number of 5-dimensional bins contributing to the individual bins of the 1-fold differential cross sections, range from 375 at $W = 1.31$ GeV to 1600 at $W > 1.38$ GeV. Summing up events in all 5-dimensional bins, reasonable statistical accuracy is achieved for the 1-fold differential cross sections (see Figs. 9, 13, ??, 19, 20). We obtained in each (W, Q^2) bin covered by measurements a set of nine 1-fold differential cross sections, consisting of $\pi^+\pi^-$, $p\pi^+$, and $p\pi^-$ mass distributions, θ_i angular distributions, as well as 3 distributions over angles α_i ($i=1,2,3$), where the index i stands for the i -th set of kinematic variables, defined in the Sect. V A. These 1-fold differential cross sections represent the integrals from the 5-fold differential cross section over four variables as:

$$\frac{d\sigma}{dM_{\pi^+\pi^-}} = \int \frac{d^5\sigma}{d^5\tau_2} d^4\tau_{\pi^+\pi^-}$$

$$d^4\tau_{\pi^+\pi^-} = dM_{\pi^-p} d\Omega_{\pi^-} d\alpha_{(p\pi^-)(p'\pi^+)};$$

$$\frac{d\sigma}{dM_{\pi^+p}} = \int \frac{d^5\sigma}{d^5\tau_2} d^4\tau_{\pi^+p}$$

$$d^4\tau_{\pi^+p} = dM_{\pi^+\pi^-} d\Omega_{\pi^-} d\alpha_{(p\pi^-)(p'\pi^+)}; \quad (8)$$

$$\frac{d\sigma}{dM_{\pi^-p}} = \int \frac{d^5\sigma}{d^5\tau_3} d^4\tau_{\pi^-p}$$

$$d^4\tau_{\pi^-p} = dM_{\pi^+\pi^-} d\Omega_{\pi^+} d\alpha_{(p\pi^+)(p'\pi^-)};$$

$$\frac{d\sigma}{d(-\cos\theta_i)} = \int \frac{d^5\sigma}{d^5\tau_i} d^4\tau_i; \quad d^4\tau_i = dM_{\pi^+\pi^-} dM_{\pi^+p} d\varphi_i d\alpha_i$$

$$\frac{d\sigma}{d(\alpha_i)} = \int \frac{d^5\sigma}{d^5\tau_i} d^4\tau_i; \quad d^4\tau_i = dM_{\pi^+\pi^-} dM_{\pi^+p} d\Omega_i.$$

In the actual cross section calculations the integrals in eq. (8) were substituted by the respective sums over the 5-dimensional kinematic bins for the hadronic cross sections.

All cross sections represent independent 1-dimensional projections of the 5-fold differential cross sections. Any of the nine 1-fold differential cross sections provides independent information and cannot be computed from the 8 remaining projections.

C. Interpolation of 5-fold differential cross section into the CLAS detector areas of zero acceptance

As discussed in Sect. IV the CLAS detector has areas with zero acceptance. The contributions from the 5-fold differential cross sections in such areas must be taken into account in order to obtain the integrated 1-fold differential cross sections. We developed a special procedure to extend the 5-fold differential cross sections in the areas of CLAS with zero acceptance.

We used the general φ_i ($i=1,2,3$) dependence of the 5-fold differential cross sections fixing the other 4 kinematic variables:

$$\frac{d^5\sigma}{d^5\tau_i} = A + B \cos 2\varphi_i + C \cos \varphi_i + B' \sin 2\varphi_i + C' \sin \varphi_i. \quad (9)$$

The first three terms are valid for any exclusive channel and for any kind of particular reaction dynamics, being a consequence of rotational invariance of the production amplitudes. The last two terms appear in the 5-fold differential cross sections for 3-body final states. After integration over the α_i angles, these two terms vanish as a consequence of parity conservation. The statistics in the populated bins is too small to allow

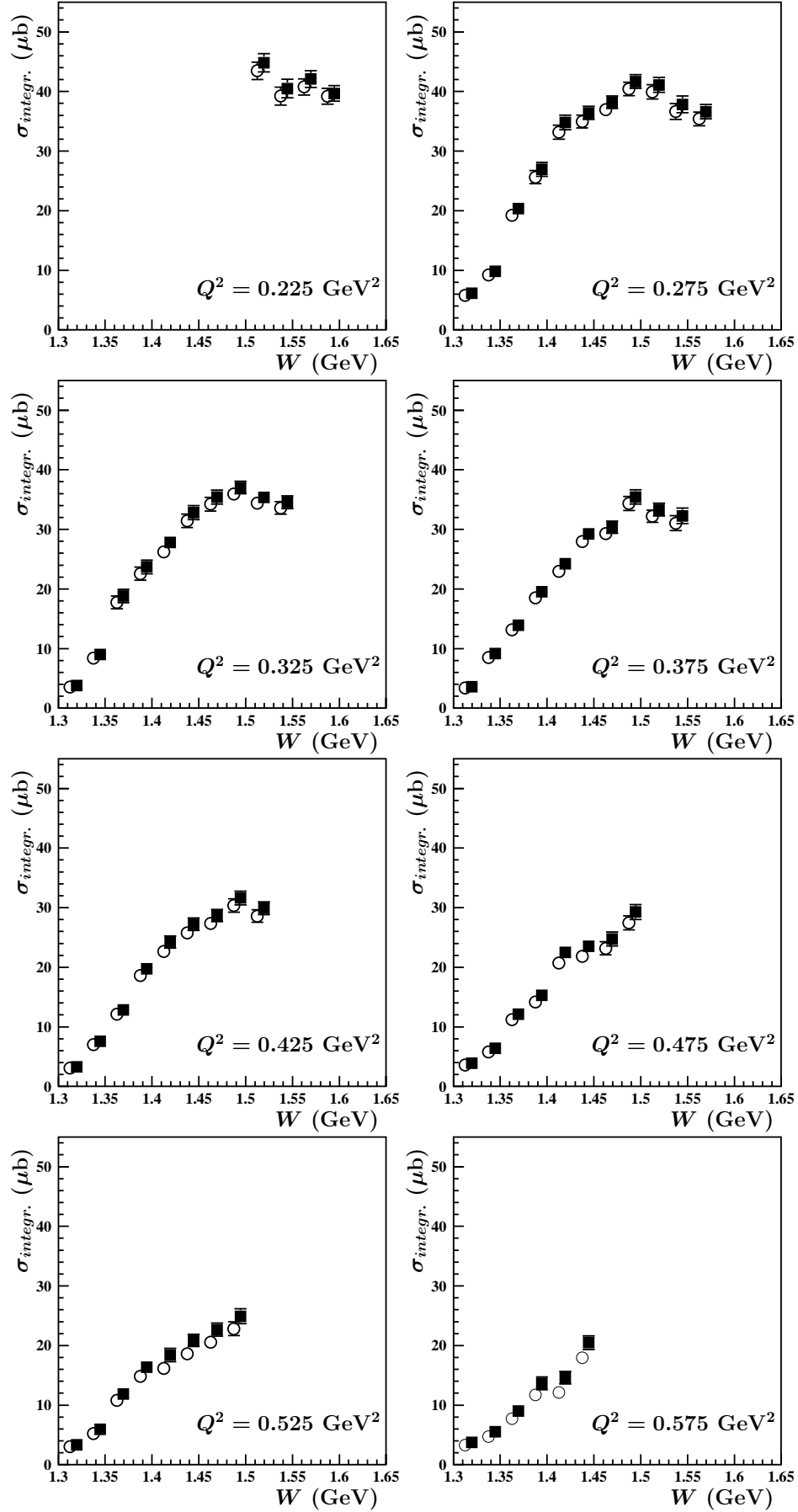


FIG. 8: Comparison of fully integrated charged double pion cross sections, obtained with (squares) and without (open circles) accounting for contributions from the CLAS areas of zero acceptance, as described in the text of Sect. V C.

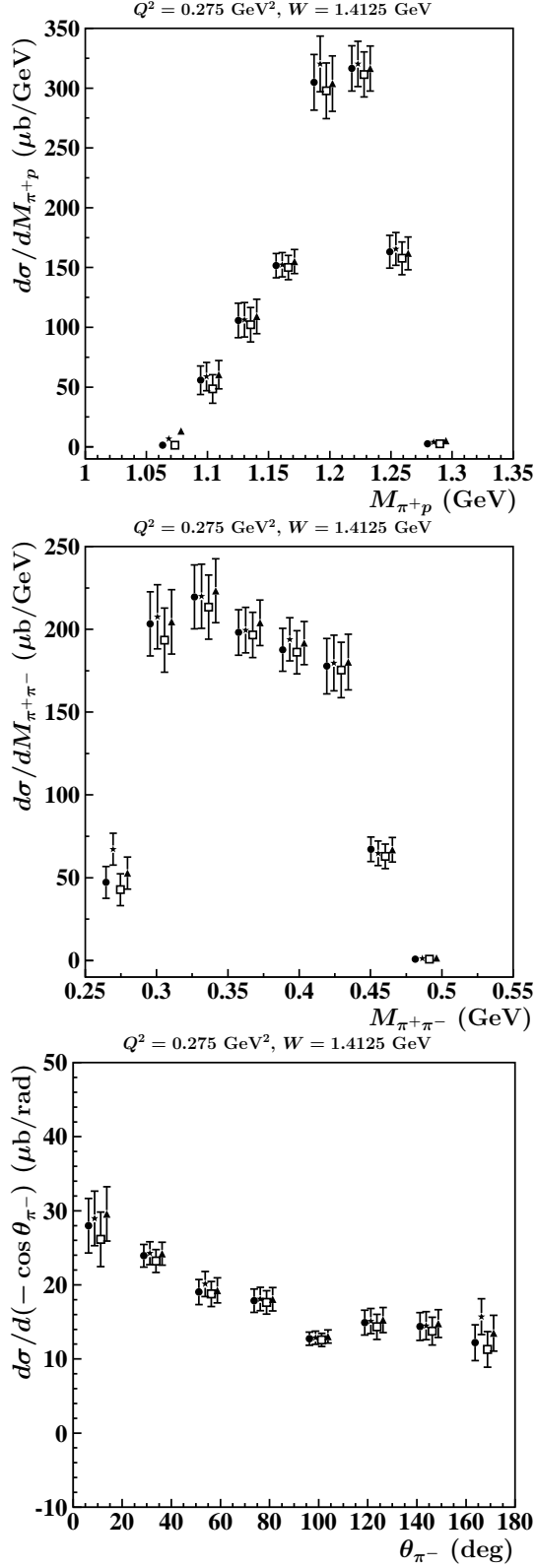


FIG. 9: Mass distributions of $p\pi^+$ (top) and $\pi^+\pi^-$ (middle), and π^- angular (bottom) distributions, obtained from different ways of interpolating the 5-fold differential cross sections into the CLAS areas of zero acceptance. Open squares correspond to 1-fold differential cross sections estimated without the contributions from the CLAS areas of zero acceptance. 1-fold differential cross sections, obtained with the R_j coefficients in eq. (10) calculated within the framework of the JM03 and JM05 models, are shown by triangles and stars, respectively. 1-fold differential cross sections, estimated by

evaluation of the A , B , C , B' , and C' coefficients from the data in the populated bins alone. Hence, we used both data and input from the models fit to the data to evaluate these coefficients. The coefficient ratios R_j ($R_1 = B/A$, $R_2 = C/A$, $R_3 = B'/A$, $R_4 = C'/A$) were taken from phenomenological models for charged double pion electroproduction fit to our data. The coefficient A was determined from the data on the 5-fold differential cross sections in the populated 5-dimensional bins $\frac{d\sigma_{meas.}}{dM_{p\pi^+}dM_{\pi^+\pi^-}d\Omega d\alpha_{(p\pi^-)(p'\pi^+)}}$ as:

$$\sum_{\Delta\varphi_{\pi^-}} \frac{d\sigma_{meas.}}{dM_{p\pi^+}dM_{\pi^+\pi^-}d\Omega d\alpha_{(p\pi^-)(p'\pi^+)}} \Delta\varphi =$$

$$A(2\pi - \Delta\tilde{\varphi}) - R_1 A \int_{\Delta\tilde{\varphi}}^{\Delta\tilde{\varphi}} \cos(2\varphi_{\pi^-}) d\varphi_{\pi^-}$$

$$- R_2 A \int_{\Delta\tilde{\varphi}}^{\Delta\tilde{\varphi}} \cos(\varphi_{\pi^-}) d\varphi_{\pi^-} - R_3 A \int_{\Delta\tilde{\varphi}}^{\Delta\tilde{\varphi}} \sin(2\varphi_{\pi^-}) d\varphi_{\pi^-} \quad (10)$$

$$- R_4 A \int_{\Delta\tilde{\varphi}}^{\Delta\tilde{\varphi}} \sin(\varphi_{\pi^-}) d\varphi_{\pi^-} ,$$

where the sum is running over the populated 5-dimensional bins, while the integrals are taken over the CLAS areas of zero acceptance $\Delta\tilde{\varphi}$. The 5-fold differential cross sections in the CLAS areas of zero acceptance were estimated from eq. (9) with coefficients A, B, C, B', C' calculated from eq. (10).

In order to determine the ratios R_j within the framework of the phenomenological models, we propagated the 5-fold differential cross sections into the CLAS areas of zero acceptance, using the JM03 model predictions for the shape of the 5-fold differential cross sections [36, 37, 38]. The parameters of the JM03 model were determined from previous CLAS charged double pion data in the resonance region [21]. In this way preliminary estimates for the 1-fold differential cross sections were obtained. Similar approaches to propagate the 5-fold differential cross sections into the CLAS areas of zero acceptance were used in previous charged double pion data analyses, published in Refs. [21, 24]. In the next step, the parameters of JM03 were further adjusted to reproduce preliminary estimates of the 1-fold differential cross sections. The R_j coefficients were calculated within the framework of the JM03 approach after mentioned adjustment of the JM03 parameters. The coefficients A for the φ independent parts of the 5-fold differential cross sections (see eq. (9)) were obtained from the data in the populated bins, according to eq. (10), using the improved estimates for R_j . Finally, the 1-fold differential charged double pion cross sections were obtained as described in Sect. VB, using the 5-fold differential cross sections in the CLAS areas of zero acceptance determined from eq. (9) with values of A , B , C , B' and C' determined as described above.

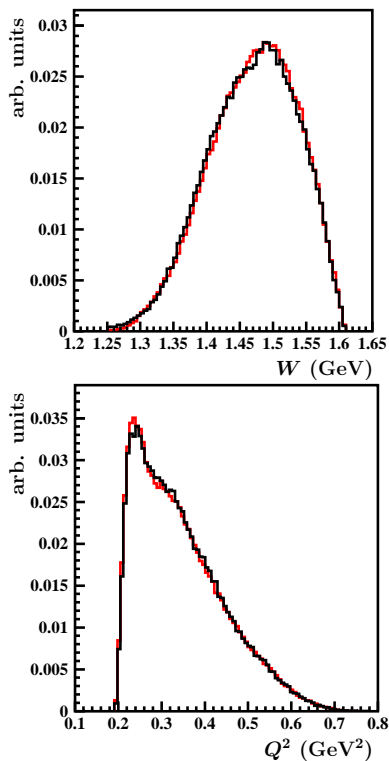


FIG. 10: (color on line) W (top panel) and Q^2 (bottom panel) distributions. The black lines represents data, and the red lines simulation.

Since the model was used to evaluate the ratios R_j , the model assumptions affect mostly the φ -dependent parts in eq. (9). After integration over φ_i angles, these parts disappear. Nevertheless, as follows from eq. (10), the model assumptions used to interpolate the charged double pion cross sections into the CLAS areas of zero acceptance will increase the uncertainties of the 1-fold differential cross sections obtained in our analysis. Detailed studies to evaluate these uncertainties were carried out and are described below.

First, we estimated the overall contribution from the inefficient areas to the 1-fold differential cross sections, calculating them in two ways: (1) by including the contributions from the areas of zero acceptance in CLAS, as described above, and (2) by excluding them. In all cases, the two sets of values were found to overlap well inside the statistical uncertainties in the entire kinematic region covered in the experiment. One example is shown in Fig 9.

In Fig 8 we show a comparison of the fully integrated charged double pion cross sections. Again, within the entire kinematic area the differences between the two sets of cross sections are well within the statistical uncertainties.

In the next step we investigate how the 1-fold differential cross sections may be affected by the model assumptions used in the procedure described above. Since only φ -independent parts of eq. (9) contribute to the 1-fold

differential cross sections, we need to know the model uncertainties just for the A coefficients. As follows from eq. (9), the influence of the φ -dependent parts on the A coefficients depend on: a) the relative contributions of the φ -dependent parts to the 5-fold differential cross sections; b) the ratio $\Delta\tilde{\varphi}/2\pi$, where $\Delta\tilde{\varphi}$ is the overall φ coverage of the CLAS areas of zero acceptance. The relative contributions from the φ -dependent parts is estimated by fitting the φ_i angular distributions^[1], using eq. (9) with A , B and C coefficients as free parameters. The φ_i angular distributions were obtained as integrals from the 5-fold differential cross sections over the other four variables. The B' and C' terms should be equal to zero since these terms are integrated over the α_i angles. The contributions from B and C in eq. (9) range from 10 % to 50 %. For the majority of bins in Q^2 and W , these contributions range from 15 % to 25 %. The upper limit for the model dependence of the A coefficients has been estimated by replacing in eq. (10) all cosines by unity and by assuming $\Delta\tilde{\varphi}/2\pi \sim 0.2$ for the geometrical coverage of the zero acceptance areas. With these assumptions we can calculate the model uncertainty of the A coefficients, as the product of the maximal contribution from the φ -dependent parts to the 5-fold differential cross section (0.5)^[2] and the geometrical coverage of the CLAS areas of zero acceptance (0.2), resulting in an upper limit of 10 %. However, this limit was obtained with extremely conservative estimates for the integrands in eq. (10), the CLAS areas of zero acceptance $\Delta\tilde{\varphi}/2\pi$, and the relative contributions of the ϕ -dependent parts. More realistic estimates, outlined below, result in uncertainties of a few percent.

In Fig. 9 we compare the results obtained using various models to estimate R_j . The JM03 and JM05 models are rather different in the description of the 5-fold differential cross sections. The JM05 approach provided a much improved treatment for the direct charged double pion electroproduction mechanisms [41]. It also contains an additional contact term that was introduced to improve the description of the $\pi\Delta$ isobar channels. The interpolations of the 5-fold differential cross sections into the inefficient areas using these two models for R_j , and in addition taking off the contributions proportional to $\sin 2\varphi$ and $\sin \varphi$, result in minor modifications well inside the statistical uncertainties.

Finally we eliminate the contributions from the φ -dependent parts in eq. (10) and estimate the A coefficients from data in the populated bins. The results are shown in Fig. 9 (diamonds). Again, the estimated cross sections are well inside the statistical uncertainties of the data.

[1] $i=1,2,3$ and stand for the set of kinematic variables, defined in Sect.V A.

[2] ratio sum of φ -dependent parts over the full cross section.

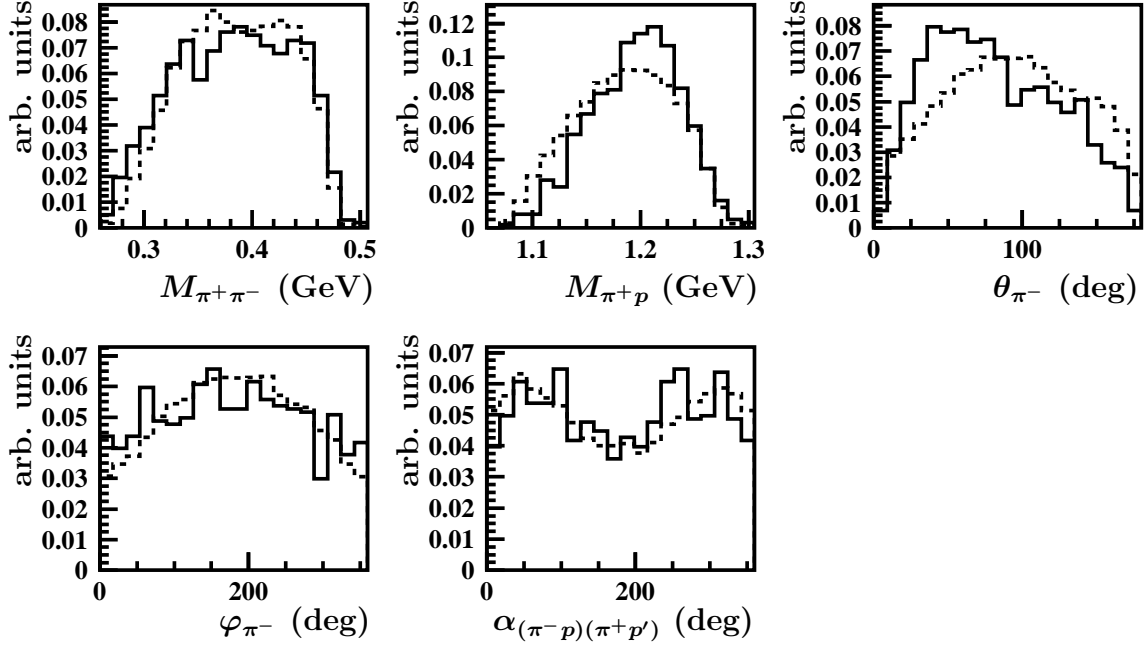


FIG. 11: Comparison between measured (solid lines) and simulated (dashed lines) event distributions for various final state variables. ($W = 1.4125$ GeV, $Q^2 = 0.525$ GeV²).

D. Event reconstruction efficiencies

A Monte Carlo event generator [63] was used to evaluate the event reconstruction efficiencies. The event generator contains the main meson production channels in the resonance region. The efficiency for detection of the $p\pi^+\pi^-$ in the final state was studied in detailed simulations that included the 2π as well as 3π final states. The latter was needed to account for multi-pion background in the selection of charged double pion events, when applying exclusivity cuts. These events were processed using the same reconstruction program [1], event selection procedures and fiducial cuts as for the events collected in the experiment. Efficiencies in the 7-fold differential bins were determined as the number of reconstructed events over the number of generated events, and used in eq. (1) to evaluate the 5-fold differential cross sections.

As can be seen from Figs. 10 and 11, the W and Q^2 dependencies are well reproduced, as are major features in the event distributions over the final state hadronic variables. Differences between the measured and simulated distributions seen for the π^+p invariant mass and π^- angular distributions have little impact as efficiencies inside these areas are smooth. The event generator is therefore adequate to evaluate the event reconstruction efficiency for major parts of the kinematic range covered

in the experiment.

The limited phase space available for events in the low mass region with $W < 1.40$ GeV requires a different approach for determining the event reconstruction efficiencies for the invariant mass distributions. In this region we found rapid variations of efficiency from invariant masses inside the bins at the lowest edges for all mass distributions. The use of an event generator that closely reflects the measured distributions is crucial in this area, where no 2π electroproduction data were previously available. Therefore, we have used an iterative procedure starting with the model event generator described above, and extracted approximate cross sections for the different mass distributions. These were then used as a realistic input into the generated event distributions over invariant masses $W_{gen}(M_k)$ ($k=\pi^+p, \pi^-\pi^+, \pi^-p$) for an accurate determination of event reconstruction efficiencies and cross sections.

The improved estimates of event reconstruction efficiencies for the mass distributions $\epsilon_{imp}(M_k)$ were obtained as:

$$\epsilon_{imp}(M_k) = \frac{W_{meas}(M_k)\epsilon(W, Q^2)}{W_{gen}(M_k)}, \quad (11)$$

where $W_{meas}(M_k)$ are event distributions in the invariant mass M_k and taken from the data. Both measured $W_{meas}(M_k)$ and generated $W_{gen}(M_k)$ ($k=\pi^+p$ event distributions were normalized to unity. The quantity $\epsilon(W, Q^2)$ is the event reconstruction efficiency in a particular (W, Q^2) -bin, and was estimated using the event generator.

[1] The correction factor that accounted for the events eliminated by the cut on the number of photoelectrons in the Cherenkov counter was applied for the measured events only.

A comparison of the mass distribution obtained using the event generator with those estimated from eq. (11) after further corrections, described in the Sect. VE, is shown in Fig. 13.

E. Corrections for mass distributions

After all of the previously discussed acceptance corrections, several mass distributions needed further corrections in order to account for the rapid variation of the cross sections inside some of the mass bins. For these bins, the cross sections were re-evaluated, using a binning size reduced by a factor of 4. Cross sections at the nominal grid were compared to those obtained at the grid of reduced bin size and interpolated into the nominal grid. In case of discrepancies, interpolated values of the cross sections were used, since they were determined with better mass resolution.

A special procedure was developed to evaluate the cross sections at the smallest invariant masses using constraints on the amplitude behavior near the phase space limits. All mass distributions at the smallest invariant masses were re-evaluated using a binning size reduced by a factor of 4 and interpolated over invariant masses in a way compatible with general requirements on a power low amplitude behavior near threshold:

$$\frac{d\sigma}{dM_k} \left[\frac{\mu b}{GeV} \right] = \begin{cases} C(M_{\pi^-p(\pi^+p)} - 1.076)^\alpha, & M_{\pi^-p(\pi^+p)} > 1.076 \text{ GeV} \\ 0, & M_{\pi^-p(\pi^+p)} < 1.076 \text{ GeV} \\ C(M_{\pi^-\pi^+} - 0.276)^\alpha, & M_{\pi^+\pi^-} > 0.276 \text{ GeV} \\ 0, & M_{\pi^+\pi^-} < 0.276 \text{ GeV} \end{cases} \quad (12)$$

where C and α are free parameters fit to the cross sections obtained with better mass resolution. The corrected cross sections were not evaluated in the mass areas closest to the threshold, which were affected considerably by the event migration. The bins of smallest invariant masses cover the mass intervals from the left edge of the next-to-smallest mass bin of reduced size to the right edge of the smallest mass bin of regular size (Fig. 12). Differential cross sections in these bins were computed as: integrals from interpolating curves inside the bins divided by the bin size ΔM . The two solid curves in Fig. 12 represent interpolating curves fit to the upper and lower boundaries of preliminary cross sections obtained with these improved mass binnings. Differences in the corrected cross sections, calculated using these two interpolations, give us the systematic uncertainties. These corrections only affect the lowest mass bins near the phase space limit. At larger invariant masses the cross sections were determined with the nominal bin size as described in the Sect. VB.

The comparison of mass distributions before and after all corrections described in Sect. VD, VE is shown in Fig 13.

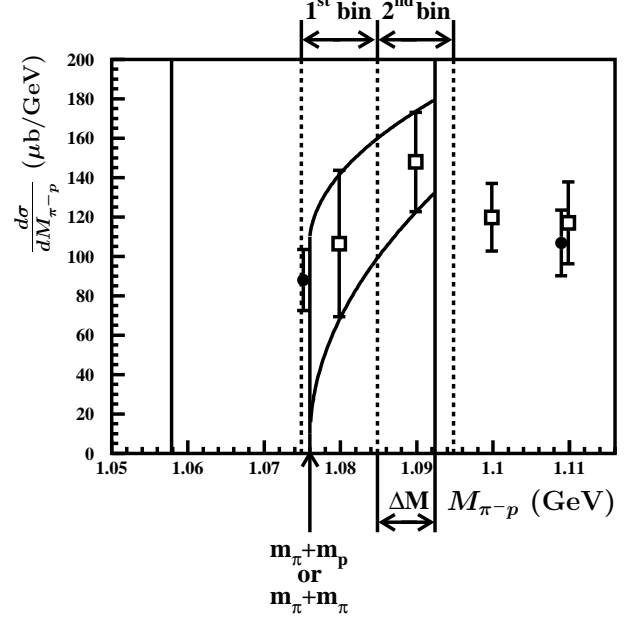


FIG. 12: Corrections for mass distribution in the cross sections near threshold. The filled circles represent the preliminary cross sections obtained with the nominal bin size. The lowest mass bin of nominal size is shown by the solid vertical lines. Preliminary cross sections obtained using a bin size reduced by a factor of 4 are shown by the open squares. The mass bins of reduced size are shown by the vertical dashed lines. The bin of lowest invariant masses ΔM , where corrected cross sections were evaluated, covers the interval from the dashed to the solid lines connected by the double sided arrow. Corrected cross sections are given by the integrals from interpolating curves inside the ΔM bin over the bin width.

F. Radiative corrections

Radiative processes were evaluated using the procedure of Mo and Tsai [67] developed for inclusive processes, and incorporated in the event generator [63]. Approaches that are capable at describing radiative processes in exclusive 2π electroproduction, are not yet available.

The radiative correction factor R was determined as:

$$R = \frac{N_{rad}}{N_{norad}}, \quad (13)$$

where N_{rad} and N_{norad} are the numbers of generated events in each (W, Q^2) bin with radiative effects switched on and off, respectively. This factor R was used in eq. (1) for calculations of the 5-fold differential cross sections.

The particular hadronic tensor for exclusive 2π electroproduction has impact mostly on radiation of the hard photons by the ingoing and scattered electrons. Moreover its influence on observables decreases after integration over the final state kinematic variables [68]. The inclusive procedure for radiative corrections represents a reasonable approximation for the case of our data, since

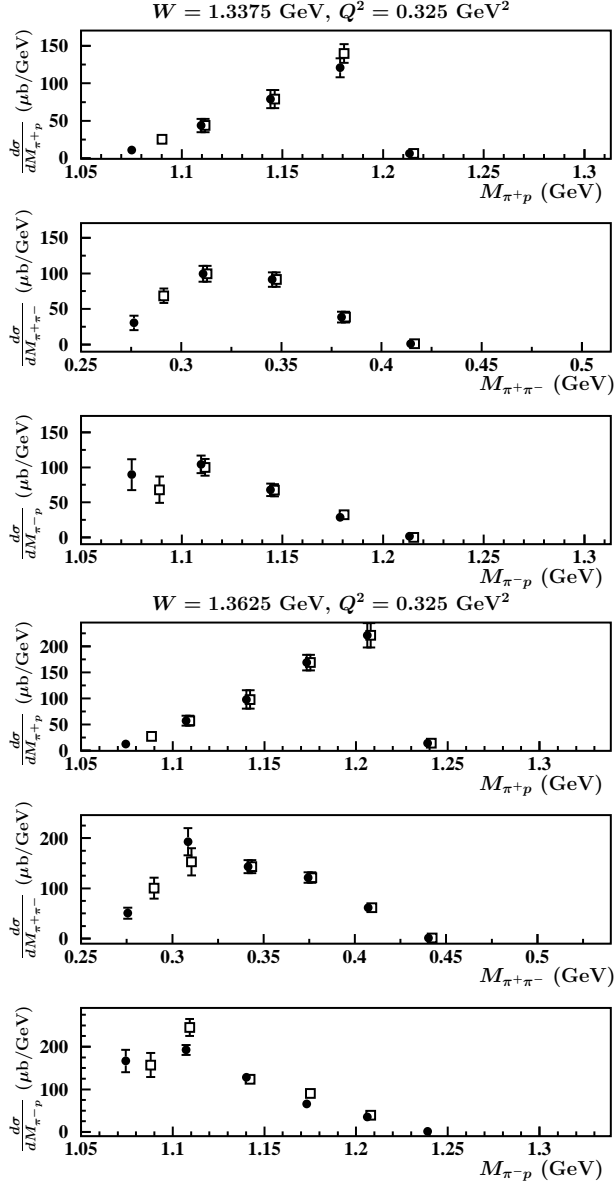


FIG. 13: Comparison of mass distribution cross sections before (filled circles) and after (open squares) improvements, described in Sect. V D, V E.

we applied an exclusivity cut, which restricts the hardness for the emitted photons, and all 1-fold differential cross sections represent integrals of the 5-fold differential cross sections over four kinematic variables.

We found that the relative contributions of hard photons to R varied from 30 to 50 %. It is only this contribution that could be affected by the hadronic tensor and may be different in various exclusive channels.

In Ref. [68] the effect of integration over kinematic variables for the case of the exclusive single pion electroproduction was studied, for which radiative processes have been evaluated exactly with the hadronic tensor derived from the fit to data. It was found that radiative correc-

tions are reduced by factors of 2 to 4 after integration over the φ angle for the emitted pion. Therefore, integration over four variables in the case of charged double pion electroproduction is expected to reduce the radiative correction factor considerably, at least by a factor of 4 [68].

Radiative corrections in the kinematics of this measurement were found to be less than 20 %. Therefore the contribution due to hard photon emission to the radiative corrections should be less than 10 %. They should be further reduced by more than a factor of 4 after integration of the 5-fold differential cross sections over four variables. Even a large uncertainty of 100 % in the contributions of hard photons would result in uncertainties of the overall radiative corrections to charged double pion cross section of only a few percent.

The uncertainty in determining the cross sections caused by using the inclusive approximation for radiative corrections is well below the statistical uncertainties of the data, and is included in the systematic uncertainties¹.

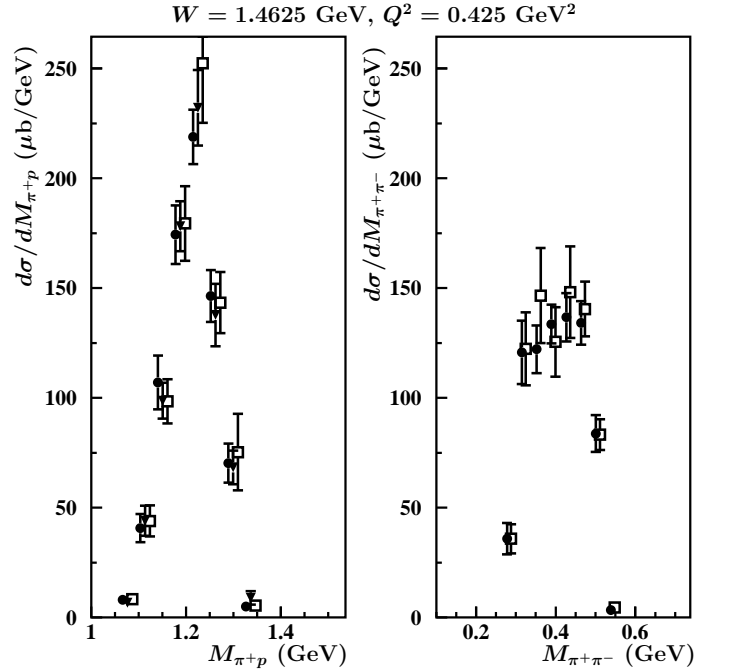


FIG. 14: Comparison between π^+p and $\pi^-\pi^+$ mass distribution cross sections, obtained by integration of the 5-fold differential cross sections for various choices of the final state kinematic variables (choices from 1 to 3 are shown by file circles, open squares and triangle respectively), defined in the Sect. V A.

[1] The information obtained on the hadronic tensor from our JM model [43] based on a fit to the charged double pion data represents valuable input for the future development of a fully exclusive radiative correction procedure for double pion electroproduction.

TABLE I: Summary of systematic uncertainties for the fully integrated cross sections. The values represent averages over the kinematic areas covered by the data.

Source	Systematic uncertainty
Integration	3 %
Fiducial cuts	3 %
Missing mass cut	2.5 %
Normalization	< 5 %
Binning effects	3 %
Radiative correction	< 3.5 %
Acceptances	3 %
Total	< 9 %

G. Results and systematic uncertainties

In our analysis we determined nine 1-fold differential cross sections in each (W, Q^2) bin at invariant masses of the hadronic system from 1.30 to 1.57 GeV and at photon virtualities from 0.2 to 0.6 GeV² with bins in W of 25 MeV and in Q^2 of 0.05 GeV². The data consist of π^+p , $\pi^-\pi^+$, and π^-p invariant mass distributions, as well as π^- , π^+ , and proton angular distributions, and 3 distributions over angles α_i ($i=1,2,3$) defined in Sect. V A. The full data set, consisting of 4695 cross sections, may be found in Ref. [23]. Fully integrated cross sections are shown in Fig. 15 and Fig. 16. These results represent the first comprehensive data set for charged double pion electroproduction at $Q^2 < 0.6$ GeV². With respect to the previous data [20], the bin size in W is reduced by almost a factor of 10, while the binning in Q^2 is reduced by a factor of 5.

Systematic uncertainties averaged over the kinematic range covered by the data are presented in Table I. In the following we discuss the various contributions to the systematic uncertainties in more detail.

To estimate uncertainties in the integration procedure, we compared the values of the fully integrated cross sections obtained by integration over three sets of kinematic variables, defined in Sect. V A. The ratios of r.m.s values for the integrated cross sections over their mean values were treated as systematics uncertainties related to the integration procedure. They are maximal at the lowest W value for all photon virtualities, and range from 5 to 7 %. As W increases, they drop to ~ 1 % at the highest W value.

In order to estimate the uncertainties in the integration procedure for the 1-fold differential cross section, we compared their values determined in integration of the 5-fold differential cross sections, obtained with three different choices of the final state variables, described in Sect. V A. When calculating these integrals for various kinematic variables, different sets of 5-dimensional bins contribute to the respective integrals. The efficiency was estimated for each set independently. Moreover, differ-

ent inefficient areas contribute to the same cross sections estimated from integration over various kinematic grids. Therefore, a comparison of fully integrated and 1-fold differential cross sections, obtained by integration over various kinematic variables, allows us to check the accuracy of the detector efficiency evaluations and propagation of the 5-fold differential cross sections in the CLAS areas of zero acceptance.

Each of the three kinematic grids, discussed in Sect. V A, contains the π^+p invariant mass distribution, while just two grids contain $\pi^-\pi^+$ invariant masses. The angles describing the final state particles have unique assignments for each of three kinematic grids. We can therefore compare the results of integrations over 3 different kinematic grids for the π^+p mass distributions. For the $\pi^-\pi^+$ mass distributions the integration over two grids can be compared. We found that these 1-fold differential cross sections coincide well within their statistical uncertainties and in the entire range of kinematics covered by measurements. As an example, in Fig. ?? we show the comparison of mass distributions at $W = 1.41$ GeV and $Q^2 = 0.425$ GeV², with the ones obtained from integrating the 5-fold differential cross sections over different sets of kinematic variables. The comparison of the fully integrated cross sections is shown in Fig. 15. The results differ by only a fraction of the statistical uncertainties.

The main contributions to the uncertainty in the overall cross section normalization are given by uncertainties in the integrated luminosity and the electron detection and reconstruction efficiencies. These contributions have been estimated by measuring the well known elastic ep scattering cross sections. The comparison with a parameterization [65] of the world data shows that the overall normalization is within a ~ 5 % uncertainty.

In order to evaluate the systematics involved in defining the final state exclusive process, we varied the missing mass cut used to identify the unmeasured π^- , and modified the fiducial regions where final state particles are selected. The average uncertainties are shown in Table I.

In Sect. V C we concluded that the contributions of the zero acceptance regions in CLAS affect the extracted differential and integrated cross sections well within the statistical uncertainties. Systematics uncertainties related to propagating the data into the inactive areas of CLAS were estimated, assuming a 50 % uncertainty in the extrapolation of the 5-fold differential cross sections, resulting in 2 % to 5 % uncertainties, and increasing in Q^2 .

The global systematics for radiative corrections, listed in the Table I, were calculated assuming the individual contributions are uncorrelated. The factor R , obtained from our Monte Carlo simulation (Sect. V F), revealed no Q^2 dependence in the entire kinematic range of our measurements. The root-mean-square values for the R factors calculated at various Q^2 were assigned to the uncertainties for the radiative correction factor. Based on the estimates described in Sect. V F, we assigned an up-

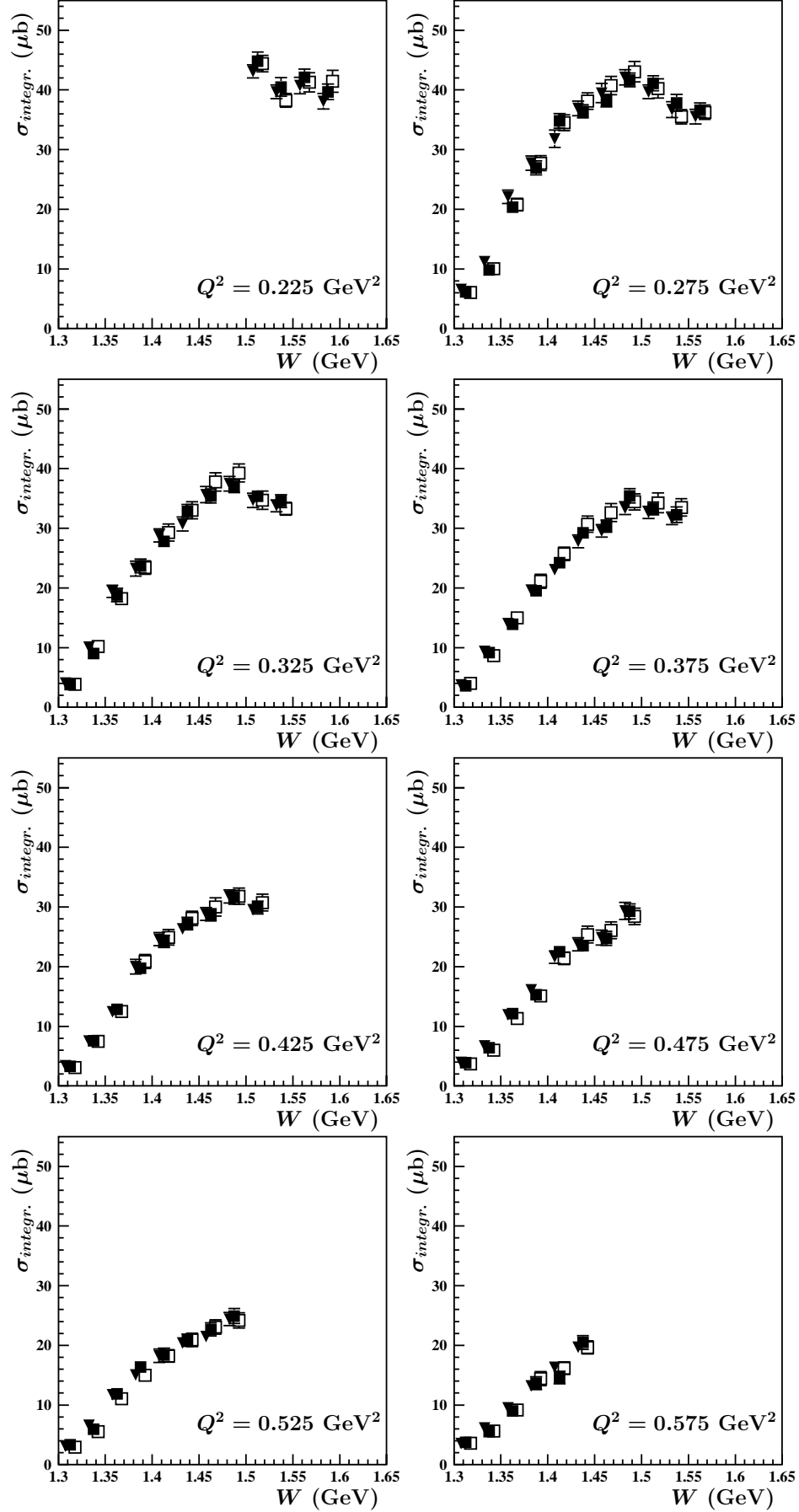


FIG. 15: Comparison between fully integrated charged double pion cross sections, obtained in the integration of the 5-fold differential cross sections over three various choices of the final state variables, described in the Sect. V A. The choices for kinematical variables from 1 to three are shown by triangles, the open and full squares respectively

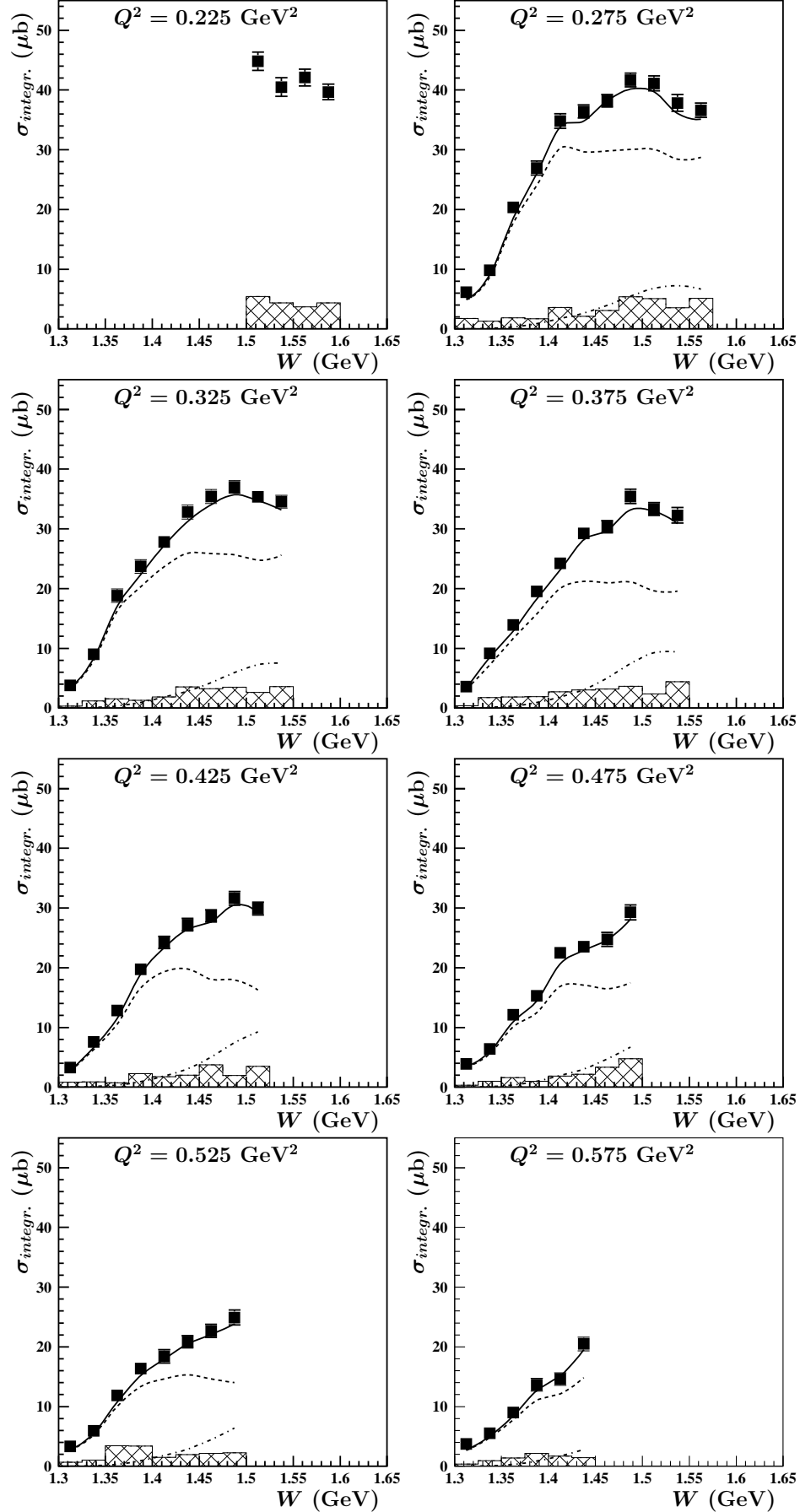


FIG. 16: Fully integrated 2π cross section at various Q^2 . Crossed areas represent systematic uncertainties. Full calculations within the framework of the JM06 model [43] are shown by solid curves. The contributions from s -channel resonances and from non-resonant mechanisms are shown by the dot-dashed and dashed curves respectively.

per limit of 2.5 % to the uncertainties related to the hard photon emission.

The overall systematic uncertainty shown in Table I was obtained as the square root of the quadratic sum over the individual contributions. Applying the described procedures in each bin of W and Q^2 individually, we obtain the systematic uncertainties for the integrated cross sections as shown by the shaded areas in Fig. 16.

VI. PHENOMENOLOGICAL ANALYSIS

The comprehensive information on the 1-fold differential cross sections for charged double pion production provided by the data enabled us to carry out a combined analysis of the nine 1-fold differential cross sections in each W and Q^2 bin, and to establish all significant mechanisms contributing to charged double pion electroproduction in the range $W < 1.6$ GeV and $Q^2 = 0.2-0.6$ GeV². Before our data were available, the information on 2π electroproduction mechanisms in this kinematic area was rather scarce and quite uncertain. Reasonable knowledge on 2π electroproduction mechanisms, achieved in our data analysis, also allowed the separation of resonant and non-resonant contributions needed for the evaluation of nucleon resonance electrocouplings.

The presence and strengths of the contributing 2π electroproduction mechanisms were established by studying the kinematical dependencies in differential cross sections and their correlations in a variety of available observables. The analysis was carried out using a phenomenological model developed in the past few years by the Jefferson Laboratory - Moscow State University (JM) collaboration [22, 41, 43, 44, 70]. Within the JM model developed up to 2005, called JM05, the major part of $\pi^+\pi^-$ production at $W < 1.6$ GeV is due to the contribution from the $\pi\Delta$ isobar channels. This is supported by the data in that the peaks from Δ^{++} (1232) resonance were clearly seen in all π^+p mass distributions at $W > 1.4$ GeV, while other mass distributions did not show any visible structures. The contributions from all other isobar channels included in JM05 become negligible in this deeply sub-threshold region of $W < 1.6$ GeV. Analysis of the recent CLAS 2π data, presented in this paper, allowed us to study manifestations of the JM05 mechanisms and search for other contributing processes in the still unexplored kinematics area of photon virtualities from 0.25 to 0.6 GeV². This analysis also enabled us to access the dynamics of the contributing mechanisms at a phenomenological level, fitting them to all measured observables combined. Our knowledge on the contributing mechanisms was extended considerably, resulting in the recent version of the JLAB-MSU model, which we refer for as JM06. A detailed description of the JM06 model version may be found in a separate paper [44]. Here we discuss the basic ingredients of JM06 and the major results.

The $\gamma^*p \rightarrow \pi^+\pi^-p$ production amplitude within the

JM05/JM06 model versions can be written as:

$$T_{\gamma^*N,\pi\pi N} = T_{\gamma^*N,\pi\pi N}^{\pi\Delta} + T_{\gamma^*N,\pi\pi N}^{dir} \quad (14)$$

with

$$T_{\gamma^*N,\pi\pi N}^{\pi\Delta} = [t_{\gamma^*N,\pi\Delta}^R + t_{\gamma^*N,\pi\Delta}^{Born} + t_{\gamma^*N,\pi\Delta}^c] \cdot G_{\Delta}\Gamma_{\Delta,\pi N}, \quad (15)$$

where G_{Δ} is a propagator of the Δ intermediate state, and the vertex function $\Gamma_{\Delta,\pi N}$ describes the $\Delta(1232) \rightarrow \pi N$ decay. The mechanisms in the above equations for the JM05 model version are illustrated in Fig.17. The diagram $\gamma N \rightarrow N^*, \Delta^* \rightarrow \pi\Delta$ in the second row of the figure is the resonant term $t_{\gamma^*N,\pi\Delta}^R$ in eq. (16). It is parameterized as a Breit-Wigner form [36] and calculated from all well established N^* states with masses less than 2.0 GeV that have hadronic decays to the $\pi\pi N$ final states. In the kinematic area covered in our measurements, only the $P_{11}(1440)$ and $D_{13}(1520)$ nucleon resonances have the contributions in 1-fold differential cross-sections, that are outside of the data uncertainties. The non-resonant term $t_{\gamma^*N,\pi\Delta}^{Born}$ is calculated from the well established Born terms of $\gamma^*N \rightarrow \pi\Delta$ [28, 36]. Their amplitudes are presented in Ref. [36, 44]. The final state interactions were treated effectively within the framework of the absorptive approximation [36]. Additional contact terms were implemented in order to account for possible contributions from other mechanisms to $\pi\Delta$ production, as well as for hadronic interactions of $\pi\Delta$ states with other open channels [41, 70]. These extra contributions to the $\pi\Delta$ isobar channels were previously established [41] in analysis of CLAS 2π data [21] and confirmed by the data of this paper. A parametrization for these amplitudes will be presented in Ref. [44]. The contributions from all isobar channels combined account for from 70 to 90 % of the 2π fully integrated cross sections in the kinematic area covered in our measurements. A remaining part of cross sections comes from direct charged double pion production mechanisms, when the $p\pi^+\pi^-$ final state is created without the formation of the intermediate quasi-two-body states with unstable hadrons. In the JM03 model version we started with a simplest parametrization for direct 2π mechanisms as the three body phase space with the amplitudes that were independent from the final state kinematic variables and fit to the data in each bin of W and Q^2 independently [37, 38]. However, this parametrization did not allow us to reproduce steep dependencies in π^- angular distributions at the backward angles, clearly seen both in the previous CLAS 2π electroproduction data [21] and in the data of this paper. The example is shown in Fig. 19,20. In order to reproduce such data behavior, the direct 2π production mechanisms were parameterized in JM05 [40, 43] in terms of a contact vertex and a unspecified particle-exchange amplitude, described by the effective propagator, which depends exponentially from a running four-momenta squared. The diagrams in the bottom of Fig.17 represents the direct term

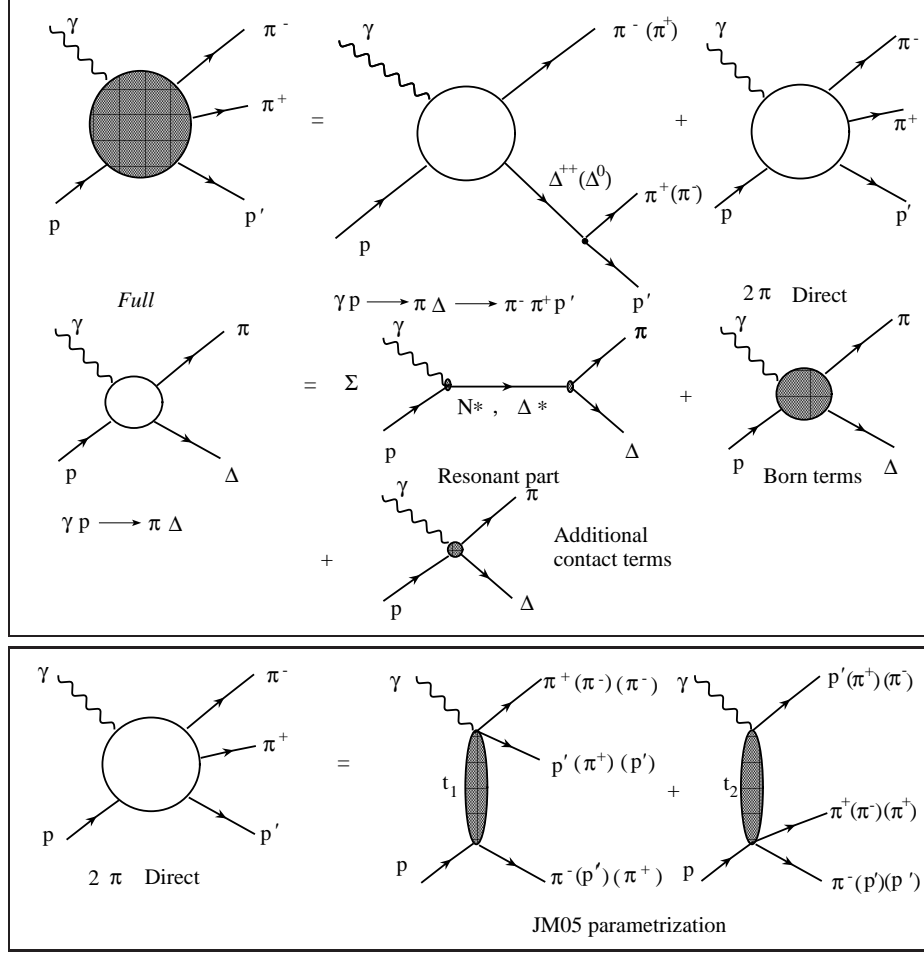


FIG. 17: The mechanisms of JM05 model [40, 41] contributing to 2- π electroproduction at low W and Q^2 .

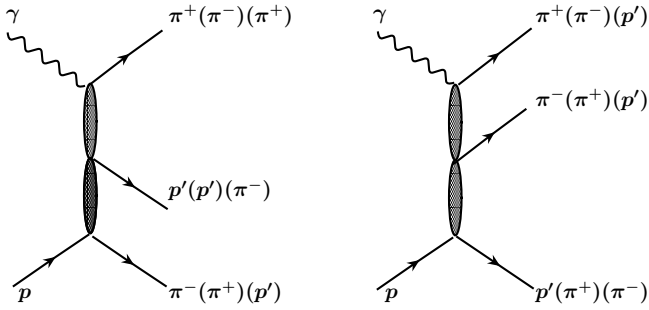


FIG. 18: Direct charged double pion production mechanisms in JM06 model.

$T_{\gamma^* N, \pi\pi N}^{dir}$ in eq.(14) that was introduced in Refs.[40, 43] to describe the direct $\gamma N \rightarrow \pi\pi N$ mechanisms. The parameterization of this term in JM05 was given explicitly in Ref. [40].

This parameterization allowed us to describe successfully the previous CLAS 2π data [21] and the data of

our paper on three invariant masses and π^- C.M. angular distributions. Analysis of nine 1-fold differential cross-sections, which was carried out for the first time, demonstrated the shortcomings in description of π^+ and p C.M. angular distributions related to the parametrization of the direct 2π electroproduction in the JM05 model [70]. Our data offer a compelling evidence for necessity to modify a description of the direct 2π production mechanisms. In the recent JM06 model version they were parameterized as two subsequent unspecified particle-exchanges amplitudes, shown in Fig. 18 for various assignments of the final state particles. Both propagators describing unspecified particle exchanges were parametrized by the same exponential dependence from a running four-momenta squared. Explicit parametrization for the amplitudes of these mechanisms will be presented in a separate paper of Ref. [44].

Within the framework of the JM06 approach we were able to describe the 2π data of our paper in the entire kinematic range covered by the measurements. As a typical example, the model description of the nine 1-

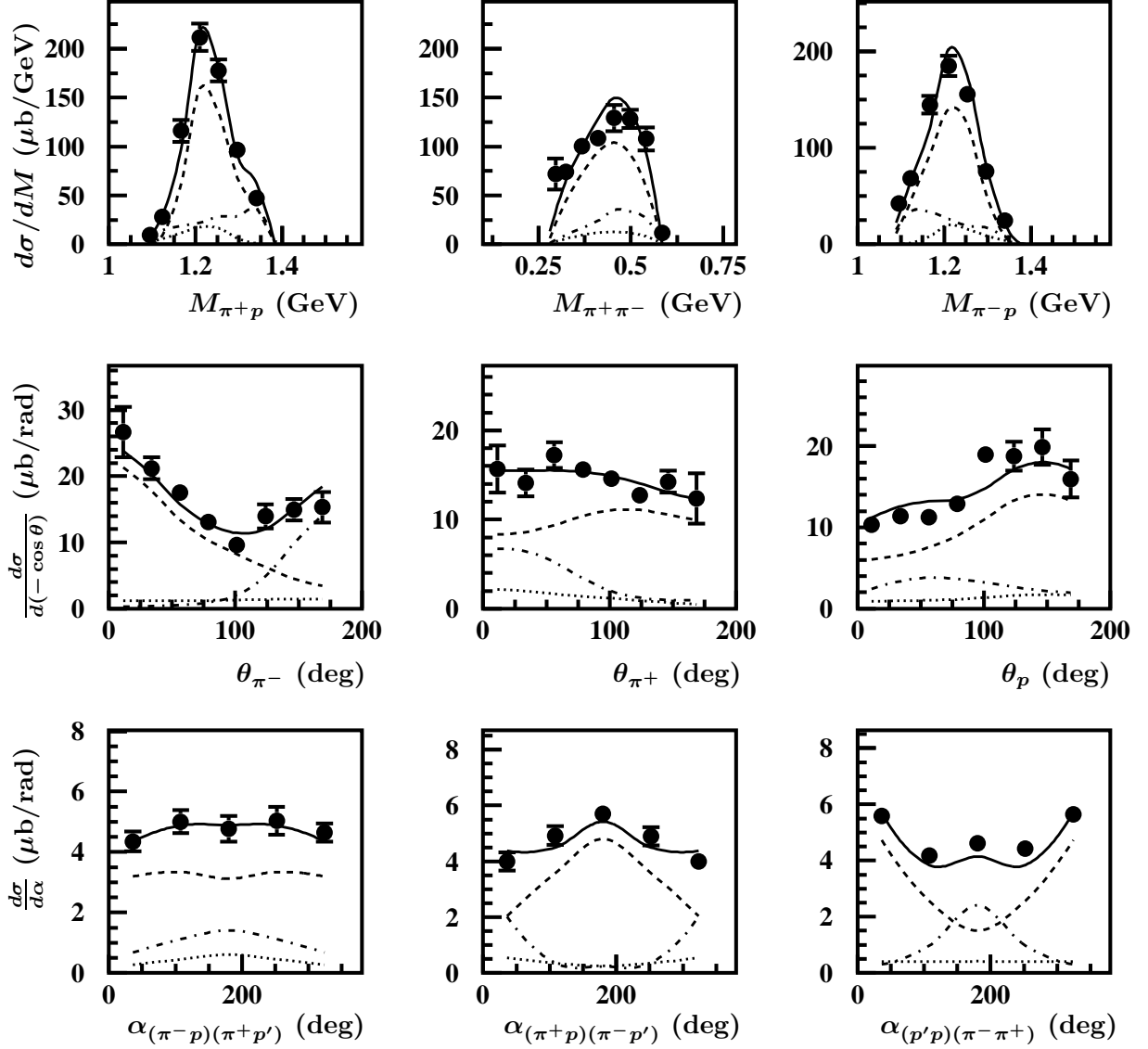


FIG. 19: Description of CLAS charged double pion differential cross sections at $W = 1.51$ GeV and $Q^2 = 0.425$ GeV² within the framework of the JM06 model. The full calculations are shown by the solid lines. The contributions from $\pi^-\Delta^{++}$ and $\pi^+\Delta^0$ isobar channels are shown by the dashed and dotted lines, respectively. The contributions from direct charged double pion production processes are shown by the dot-dashed lines. α_i angular distributions were calculated with the JM06 parameters fit to the other 6 differential cross sections.

fold differential charged double pion cross sections at $W = 1.51$ GeV and $Q^2 = 0.425$ GeV² is shown in Fig. 19 together with the contributions of all mechanisms incorporated in the JM06 description.

The shapes of the cross sections for the different mechanisms are substantially different in the various observables, but highly correlated by the reaction dynamics. Moreover, we found no need to implement additional mechanisms beyond the ones already included in JM06. Therefore, the successful description of all nine 1-fold differential charged double pion cross sections allowed us to identify all significant contributing processes and access their dynamics at the phenomenological level. To check

the robustness of the results obtained within the framework of the JM06 model, we fit the model parameters to a limited set of data that included only six differential cross sections: all three invariant masses and three angular θ_i ($i=\pi^-, \pi^+, p$) distributions for the final state hadrons. The remaining three distributions over the α_i angles were calculated, keeping the JM06 parameters fixed. A good description of all of the α_i distributions was achieved throughout the kinematics covered by the measurements, giving us confidence that the main processes are described within the JM06 model.

The separated resonant and non-resonant contributions to the fully integrated cross sections are also pre-

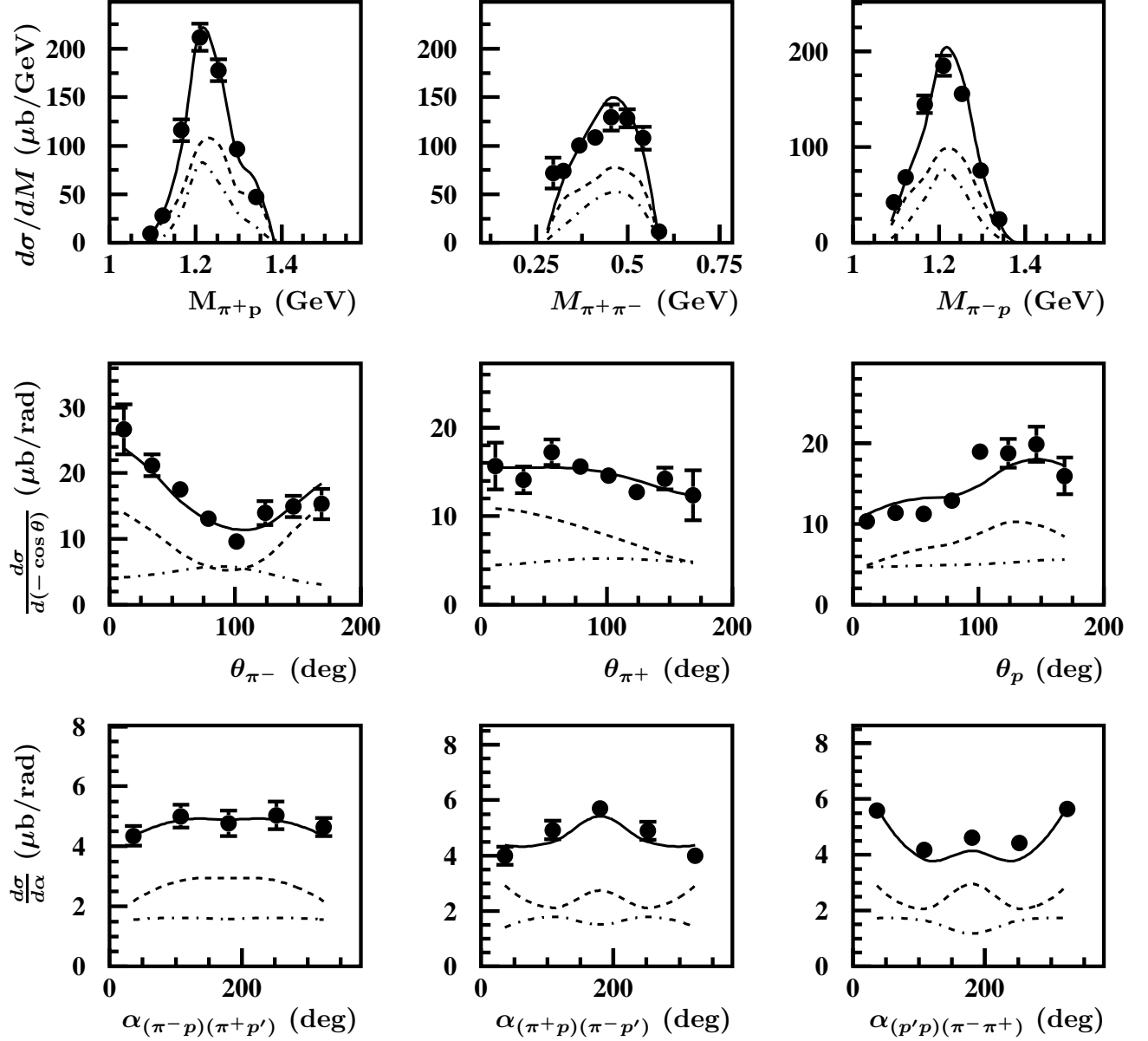


FIG. 20: Resonant (dot-dashed lines) and non-resonant (dashed lines) contributions to the charged double pion differential cross sections at $W=1.51$ GeV and $Q^2=0.425$ GeV². The full JM06 calculations are shown by black solid lines.

sented in Fig. 16. The resonant and non-resonant parts of the differential cross sections at $W = 1.51$ GeV and $Q^2 = 0.425$ GeV² are shown in Fig. 20. Non-resonant mechanisms represent a major contributor in entire kinematic area covered by our measurements. The relative resonant contributions increase with Q^2 but remains below than 30 %. However, the resonant contributions increase rapidly at $W > 1.4$ GeV, where they become larger than the data uncertainties and may be determined from the data fit. The dominant part of the resonant amplitudes comes from the $P_{11}(1440)$ and $D_{13}(1520)$ states combined. The phase space limitations prevent $P_{33}(1232)$ decays to the final states with two pions. There is also no evidence

for substantial decays of the $S_{11}(1535)$ resonance with two pion emission, while the tail from the nucleon excitations with masses above 1.6 GeV is well inside the data uncertainties.

The shapes of the resonant and non-resonant contributions are quite different for most differential cross sections, especially the angular distributions. Moreover, the correlations between kinematical dependencies of the resonant/non-resonant parts in various 1-fold differential cross-sections are also quite different. Therefore, a reasonable description of all differential cross sections combined, which is achieved within the framework of the JM06 model, provides an evidence that a proper isola-

tion of the resonance contributions can be obtained from global fits to all available cross section data, even in a case of relatively small ($< 30\%$) resonant contributions to the fully integrated cross-sections. It may be seen in Fig. 20, where derived from the data fit the resonant contributions are presented.

While the evaluation of N^* electrocouplings is outside the scope for this paper, it is nevertheless noteworthy that our data open up the possibility to determine electrocouplings for $P_{11}(1440)$ and $D_{13}(1520)$ states at $Q^2 < 0.6 \text{ GeV}^2$ from double pion electroproduction for the first time. The preliminary results may be found in the Ref. [70]. The kinematical region of low photon virtualities is expected to be particularly sensitive to meson-baryon dressing effects in the resonance structure [45, 49].

Moreover, in this kinematic region there are also CLAS data on single pion electroproduction [4, 6, 7, 8, 9, 23, 69]. At $W < 1.5 \text{ GeV}$ only single and double pion exclusive channels contribute to the total meson production cross sections off protons. The amplitudes for various non-resonant mechanisms contributing to single and double pion electroproduction, obtained in a phenomenological analysis of CLAS data with the framework of the JM06 model [44], represent valuable information for the study of nucleon resonance transitions in combined analyses of these major channels. Advanced coupled-channel approaches are under development at the Excited Baryon Analysis Center (EBAC) at Jefferson Lab [46, 48]. Phenomenological analysis of the double pion data of this paper, described in detail in Ref. [44], is of particular interest for this activity.

VII. CONCLUSIONS

In this paper we have presented a large body of electroproduction data for the process $\gamma_v p \rightarrow p\pi^+\pi^-$. The large acceptance of CLAS allowed extraction of the 1-fold differential and fully integrated charged double pion cross sections. The results were tested for robustness by using different integration grids, that showed that consistent results are obtained independent of the specific integration procedure.

1-fold differential and fully integrated cross sections were obtained for W from 1.3 GeV to 1.6 GeV and Q^2 from 0.2 GeV^2 to 0.6 GeV^2 . The high statistics and good momentum resolution of the measurements allowed us to use bin sizes of $\Delta W = 25 \text{ MeV}$ and $\Delta Q^2 = 0.05 \text{ GeV}^2$, which are at least a factor of 5 smaller than the ones used in previous measurements. For the first time, nine independent differential cross sections in each bin of W and Q^2 were measured.

The phenomenological analysis of the cross sections within the framework of the JM06 approach [43, 44] allowed us to establish significant mechanisms contributing to charged double pion electroproduction for the kinematics covered by our measurement. All differential and fully integrated cross sections obtained in our measure-

ment can be reasonably described by the contributions from $\pi\Delta$ isobar channels and direct double pion production mechanisms, established from phenomenological analysis of our data. The analysis of resonance contributions to the differential cross sections indicates that these data are sensitive to the resonant parts of cross-sections, allowing us to study the excitation of $P_{11}(1440)$ and $D_{13}(1520)$ states by virtual photons off protons at $Q^2 < 0.6 \text{ GeV}^2$.

The data also allowed us to determine cross sections and amplitudes for isobar channels, offering valuable information for nucleon resonance studies in a global analysis of the major meson electroproduction exclusive reactions within the framework of an advanced coupled-channel approach currently under development in EBAC at Jefferson Lab [46, 48].

VIII. ACKNOWLEDGMENTS

We would like to acknowledge the outstanding efforts of the staff of the Accelerator and the Physics Divisions at JLab that made this experiment possible. This work was supported in part by the Skobeltsyn Institute of Nuclear Physics and Physics Department at Moscow State University, the U.S. Department of Energy and the National Science Foundation, the U.K. Engineering and Physical Science Research Council, the Istituto Nazionale di Fisica Nucleare, the French Centre National de la Recherche Scientifique, the French Commissariat à l'Energie Atomique, and the Korean Science and Engineering Foundation. Jefferson Science Associates (JSA) operates the Thomas Jefferson National Accelerator Facility for the United States Department of Energy under contract DE-AC05-06OR23177.

-
- [1] V. D. Burkert, in "Electromagnetic Interactions and Hadronic Structure", ed by F. Close, 77 (2007).
- [2] V. D. Burkert, Prog. Part Nucl. Phys. **55**, 108 (2005).
- [3] V. Burkert and T. S.-H. Lee, Int. J. Mod. Phys. **E13**, 1035 (2004).
- [4] K. Joo et al., Phys. Rev. Lett. **88**, 122001 (2002).
- [5] M. Ungaro et al., Phys. Rev. Lett. **97**, 112003 (2006).
- [6] K. Joo et al., Phys. Rev. **C68**, 032201 (2003).
- [7] K. Joo et al., Phys. Rev. **C70**, 042201 (2004).
- [8] K. Joo et al., Phys. Rev. **C72**, 058202 (2005).
- [9] H. Egiyan et al, Phys. Rev. **C73**, 025204 (2006).
- [10] A. Biselli et al., Phys. Rev. **C68**, 035202 (2003).
- [11] A. Biselli et al., arXiv: 0804.3079.
- [12] K. Park et al., Phys. Rev. **C77**, 015208 (2008).
- [13] R. Thompson et al., Phys. Rev. Lett. **86**, 1702 (2001).
- [14] H. Denizli et al., Phys. Rev. **C76**, 015204 (2007).
- [15] P. Ambrozewicz et al., Phys. Rev. **C75**, 045203 (2007).
- [16] I. Aznauryan et al., arXiv: 0804.0447.
- [17] D. Carman et al., Phys. Rev. Lett. **90**, 131804 (2003).
- [18] R. De Vita et al., Phys. Rev. Lett. **88**, 082001 (2002).
- [19] G. Penner and U. Mosel, Phys. Rev. **C65**, 055202 (2002).
- [20] K. Wacker et al., Nucl. Phys. **B144**, 269 (1978).
- [21] M. Ripani et al., Phys. Rev. Lett. **91**, 022002 (2003).
- [22] G. V. Fedotov et al., Bull. of Russian Acad. of Science **71**, 328 (2007).
- [23] <http://clasweb.jlab.org/physicsdb/>. CLAS Physics Data Base.
- [24] C. Hadjidakis et al., Phys. Lett. **B106**, 256 (2005).
- [25] M. Bellis et al., Proceedings of NSTAR2004 workshop, March 24-27 2004, Grenoble, France, World Scientific, ed. by J.-P. Bocquet, V. Kuznetsov, D. Rebreyend.
- [26] U. Thoma, Int. J. Mod. Phys. **A20**, 280 (2005).
- [27] A. Anisovich, E. Klempt, A. Sarantsev and U. Thoma, Eur. Phys. J. **A24**, 111 (2005).
- [28] D. Luke and P. Söding Springer Tracts in Modern Physics 59, (1971).
- [29] J. A. Gomez Tejedor and E. Oset, Nucl. Phys. **A600**, 413 (1996).
- [30] J. C. Nacher et al., Nucl. Phys. **A695**, 295 (2001).
- [31] L. Y. Murphy and J.-M. Laget, DAPNIA-SPHN-96-10.
- [32] W. Roberts and A. Rakotovao, JLAB-TH-97-01.
- [33] W. Roberts and T. Oed, Phys. Rev. **C71**, 055201 (2005).
- [34] M. Hirata, N. Katagiri and T. Takaki, Phys. Rev. **C67**, 034601 (2003).
- [35] A. Fix and H. Arenhovel, Eur. Phys. J. **A25**, 115 (2005).
- [36] M. Ripani et al., Nucl. Phys. **A672**, 220 (2000).
- [37] V. Mokeev et al., Phys. Atom. Nucl. **64**, 1292 (2001).
- [38] V. Mokeev et al., Phys. Atom. Nucl. **66**, 1322 (2003).
- [39] V. I. Mokeev et al., Proc. of NSTAR2004 Workshop, March 24-27, 2004, Grenoble, France, ed. by J.-P. Bocquet, V. Kuznetsov, D. Rebreyend.
- [40] I. G. Aznauryan et al., Phys. Rev. **C72**, 045201 (2005).
- [41] V. I. Mokeev, V. D. Burkert, et al., Proc. of the Workshop on the Physics of Excited Nucleon. NSTAR2005, ed. by S. Capstick, V. Crede, P. Eugenio.
- [42] V. D. Burkert, et al., Phys. Atom. Nucl. **70**, 427 (2007).
- [43] V. I. Mokeev and V. D. Burkert, J. Phys. Conf. Ser **69**, 012019 (2007).
- [44] V. I. Mokeev et al., in preparation for Phys. Rev. C.
- [45] T. Sato and T.-S. H. Lee, Phys. Rev. **C63**, 055201 (2001).
- [46] A. Matsuyama, T. Sato and T.-S. H. Lee, Phys. Rep. **439**, 193 (2007).
- [47] T. S.-H. Lee, J. Phys. Conf. Ser. **69**, 012013 (2007).
- [48] T. S.-H. Lee and L. C. Smith, J. Phys. **G34**, S83 (2007).
- [49] B. Julia-Diaz et al., Phys. Rev. **C77**, 045205 (2008).
- [50] S. Capstick and B. D. Keister, Phys. Rev. **D51**, 3598 (1995).
- [51] F. Cano and P. González, Phys. Lett. **B431**, 270 (1998).
- [52] I. G. Aznauryan, Phys. Rev. **C76**, 025212 (2007).
- [53] T. Ebata and K. E. Lassia, Phys. Rev. **183**, 1425 (1969).
- [54] T. Kitagiki et al., Phys. Rev. **D34**, 2554 (1986).
- [55] J. Bell et al., Phys. Rev. Lett. **41**, 1008 (1978).
- [56] D. Allasia et al., Nucl. Phys. **B343**, 285 (1990).
- [57] C. Alexandrou et al., Phys. Rev. Lett. **98**, 052003 (2007).
- [58] B. Mecking et al., Nucl. Inst. and Meth. **A503**, 513 (2003).
- [59] M. D. Mestayer et al., Nucl. Inst. and Meth. **A449**, 81 (2000).
- [60] G. Adams et al., Nucl. Inst. and Meth. **A465**, 414 (2001).
- [61] E. S. Smith et al., Nucl. Inst. and Meth. **A432**, 265 (1999).
- [62] M. Amarian et al., Nucl. Inst. and Meth. **A460**, 239, (2001).
- [63] http://www.jlab.org/~golovach/www_eg/index.html
- [64] E. Byckling and K. Kajantie, Particle Kinematics, John Wiley & Sons Inc. 1972, New York.
- [65] P. E. Bosted et al., Phys. Rev. **C51**, 409 (2002).
- [66] E. Amaldi, S. Fubini and G. Furlan, Pion Electroproduction. Springer Tracts in Modern Physics **83**, (1989).
- [67] L. W. Mo and Y. S. Tsai, Rev. Mod. Phys. **41**, 205 (1969).
- [68] A. Afanasev et al., Phys. Rev. **D66**, 074004 (2002).
- [69] I. G. Aznauryan et al., Phys. Rev. **C71**, 015201 (2005).
- [70] V. I. Mokeev et al., Proceedings of the 11th Workshop on the Physics of Excited Nucleons. NSTAR2007, Springer, ed. by H-W. Hammer, V. Kleber, U. Thoma, H. Schmieden.

APPENDIX A: KINEMATICS VARIABLES FOR 5-DIFFERENTIAL 2- π PRODUCTION CROSS-SECTIONS

In this appendix we present the final state kinematics for the second choice of variables defined in Sect. V A. Since all momenta are measured in the lab frame, first we boost the 3-momenta of the final state particles in the c.m. frame. All 3-momenta used below, if not specified otherwise, are defined in the c.m. frame.

$M_{\pi^+\pi^-}$, M_{π^+p} and M_{π^-p} invariant masses were related to the four momenta of the final particles as:

$$\begin{aligned} M_{\pi^+\pi^-} &= \sqrt{(P_{\pi^+} + P_{\pi^-})^2} \\ M_{\pi^+p'} &= \sqrt{(P_{\pi^+} + P_{p'})^2} \\ M_{\pi^-p'} &= \sqrt{(P_{\pi^-} + P_{p'})^2}, \end{aligned} \quad (16)$$

where P_i ($i=\pi^-, \pi^+, p$) stand for the final state particle four-momenta.

The angle θ_{π^-} between the 3-momentum of the initial photon and the final state π^- in the c.m. frame was calculated as:

$$\theta_{\pi^-} = \text{acos} \left(\frac{(\vec{P}_{\pi^-} \cdot \vec{P}_{\gamma})}{|\vec{P}_{\pi^-}| |\vec{P}_{\gamma}|} \right). \quad (17)$$

The angle φ_{π^-} was determined as:

$$\varphi_{\pi^-} = \text{arctg} \left(\frac{P_{y\pi^-}}{P_{x\pi^-}} \right); P_{x\pi^-} > 0; P_{y\pi^-} > 0 \quad (18)$$

$$\varphi_{\pi^-} = \text{arctg} \left(\frac{P_{y\pi^-}}{P_{x\pi^-}} \right) + 2\pi; P_{x\pi^-} > 0; P_{y\pi^-} < 0 \quad (19)$$

$$\varphi_{\pi^-} = \text{arctg} \left(\frac{P_{y\pi^-}}{P_{x\pi^-}} \right) + \pi; P_{x\pi^-} < 0; P_{y\pi^-} < 0 \quad (20)$$

$$\varphi_{\pi^-} = \text{arctg} \left(\frac{P_{y\pi^-}}{P_{x\pi^-}} \right) + \pi; P_{x\pi^-} < 0; P_{y\pi^-} > 0 \quad (21)$$

$$\varphi_{\pi^-} = \pi/2; P_{x\pi^-} = 0; P_{y\pi^-} > 0 \quad (22)$$

$$\varphi_{\pi^-} = 3\pi/2; P_{x\pi^-} = 0; P_{y\pi^-} < 0. \quad (23)$$

The calculation of the angle $\alpha_{(\pi^-p)(\pi^+p')}$ between the two planes A and B (see Fig. 7) is more complicated. First we determine two auxiliary vectors $\vec{\gamma}$ and $\vec{\beta}$. The vector $\vec{\gamma}$ is the unit vector perpendicular to the \vec{P}_{π^-} 3-momentum, directed toward the vector $-\vec{n}_z$ and situated in the plane composed by the virtual photon 3-momentum and the π^- 3-momentum \vec{P}_{π^-} (see Fig. 7). \vec{n}_z is the unit vector directed along the z -axis (see Fig. 7). The vector $\vec{\beta}$ is the unit vector perpendicular to the 3-momentum of π^- , directed toward the π^+ 3-momentum \vec{P}_{π^+} and situated in the plane composed by the π^+ and p' 3-momenta. Note that the 3-momenta of the π^+ , π^- and p' are in the same plane, since in the center-of-mass their total 3-momentum should be equal to zero. Then the angle between the two planes $\alpha_{(\pi^-p)(\pi^+p')}$ is:

$$\alpha_{(\pi^-p)(\pi^+p')} = \text{acos}(\tilde{\gamma}/\tilde{\beta}), \quad (24)$$

with the acos function running between zero and π , and the angle between the planes A and B running from zero to 2π . To determine α in a range between π and 2π , we look at the relative orientation of the vector \vec{P}_{π^-} and vector product $\vec{\delta}$ for the auxiliary vectors $\vec{\gamma}$ and $\vec{\beta}$:

$$\vec{\delta} = \vec{\gamma} \times \vec{\beta}. \quad (25)$$

If $\vec{\delta}$ is collinear to \vec{P}_{π^-} , $\alpha_{(\pi^-p)(\pi^+p')}$ is determined from eq. (24). In the case of anti-collinear vectors $\vec{\delta}$ and \vec{P}_{π^-} :

$$\alpha_{(\pi^-p)(\pi^+p')} = 2\pi - \text{acos}(\tilde{\gamma}/\tilde{\beta}). \quad (26)$$

The vector $\vec{\gamma}$ may be expressed through the particle 3-momenta as:

$$\begin{aligned} \vec{\gamma} &= a_{\alpha}(-\vec{n}_z) + b_{\alpha}\vec{n}_{P_{\pi^-}} \\ a_{\alpha} &= \sqrt{\frac{1}{1 - (\vec{n}_{P_{\pi^-}}(-\vec{n}_z))^2}} \\ b_{\alpha} &= -(\vec{n}_{P_{\pi^-}}(-\vec{n}_z))a_{\alpha}, \end{aligned} \quad (27)$$

where $\vec{n}_{P_{\pi^-}}$ is the unit vector directed along the π^- 3-momentum (see Fig. 7). Taking scalar products $(\vec{\gamma}\vec{n}_{P_{\pi^-}})$ and $(\vec{\gamma}\vec{\gamma})$, it is straightforward to verify that $\vec{\gamma}$ is the unit vector perpendicular to \vec{P}_{π^-} .

The vector $\vec{\beta}$ may be obtained as:

$$\begin{aligned} \vec{\beta} &= a_{\beta}\vec{n}_{P_{\pi^+}} + b_{\beta}\vec{n}_{P_{\pi^-}} \\ a_{\beta} &= \sqrt{\frac{1}{1 - (\vec{n}_{P_{\pi^+}}\vec{n}_{P_{\pi^-}})^2}} \\ b_{\beta} &= -(\vec{n}_{P_{\pi^+}}\vec{n}_{P_{\pi^-}})a_{\beta}, \end{aligned} \quad (28)$$

where $\vec{n}_{P_{\pi^+}}$ is the unit vector directed along the π^+ 3-momentum. Again, taking scalar products $(\vec{\beta}\vec{n}_{P_{\pi^-}})$ and $(\vec{\beta}\vec{\beta})$, it is straightforward to see that $\vec{\beta}$ is the unit vector perpendicular to the π^- 3-momentum. The angle $\alpha_{(\pi^-p)(\pi^+p')}$ coincides with the angle between the vectors $\vec{\gamma}$ and $\vec{\beta}$. So, the scalar product $(\vec{\gamma}\vec{\beta})$ allows determination of the angle $\alpha_{(\pi^-p)(\pi^+p')}$ in eq. (24).

The kinematic variables for other hadron assignments for the first, second and third final state particle described above, were evaluated in a similar way.